Advances in Water Resources 147 (2021) 103759

Contents lists available at ScienceDirect

Advances in Water Resources

journal homepage: www.elsevier.com/locate/advwatres

Verification benchmarks for single-phase flow in three-dimensional fractured porous media

Inga Berre[a], Wietse M. Boon[b], Bernd Flemisch[c,*], Alessio Fumagalli[a,d], Dennis Gläser[c], Eirik Keilegavlen[a], Anna Scotti[d], Ivar Stefansson[a], Alexandru Tatomir[e,f], Konstantin Brenner[g], Samuel Burbulla[h], Philippe Devloo[i], Omar Duran[i], Marco Favino[j], Julian Hennicker[k], I-Hsien Lee[l,m], Konstantin Lipnikov[n], Roland Masson[g], Klaus Mosthaf[o], Maria Giuseppina Chiara Nestola[p], Chuen-Fa Ni[l,m], Kirill Nikitin[q], Philipp Schädle[r], Daniil Svyatskiy[n], Ruslan Yanbarisov[q], Patrick Zulian[p]

[a] Department of Mathematics, University of Bergen, Allégaten 41, Bergen 5007, Norway
[b] Department of Mathematics, KTH Royal Institute of Technology, Lindstedtsvägen 25, Stockholm 11428, Sweden
[c] Department of Hydromechanics and Modelling of Hydrosystems, University of Stuttgart, Pfaffenwaldring 61, Stuttgart 70569, Germany
[d] Laboratory for Modeling and Scientific Computing MOX, Politecnico di Milano, p.za Leonardo da Vinci 32, Milano 20133, Italy
[e] Department of Applied Geology, Geosciences Center, University of Göttingen, Goldschmidtstrasse 3, Göttingen 3707, Germany
[f] Department of Earth Sciences, Uppsala University, Villavägen 16, Uppsala S-75236, Sweden
[g] University of Côte d'Azur, CNRS, INRIA, LJAD, Nice, France
[h] Institute of Applied Analysis and Numerical Simulation, University of Stuttgart, Pfaffenwaldring 57, Stuttgart 70569, Germany
[i] FEC-Universidade Estadual de Campinas, R. Josiah Willard Gibbs 85 - Cidade Universitária, Campinas SP, Brazil, CEP 13083-839
[j] Institute of Earth Sciences, University of Lausanne, Building Geopolis, UNIL-Mouline, Lausanne 1015, Switzerland
[k] Section de Mathématiques, University de Genève, 2–4 rue du Liévre, CP 64, Genève 1211, Switzerland
[l] Graduate Institute of Applied Geology, National Central University, Taiwan
[m] Center for Environmental Studies, National Central University, Taiwan
[n] Los Alamos National Laboratory, New Mexico, USA
[o] Department of Environmental Engineering, Technical University of Denmark, Bygningstorvet, Building 115, Lyngby 2800 Kgs., Denmark
[p] Numerical Simulation in Science, Medicine and Engineering Group, Institute of Computational Science, University della Svizzera italiana Via G. Buffi 13, Lugano Ticino 6900, Switzerland
[q] Marchuk Institute of Numerical Mathematics of Russian Academy of Sciences, Moscow, Russia
[r] ETH Zürich, Geothermal Energy and Geofluids Group, Institute of Geophysics, Zürich 8092, Switzerland

A B S T R A C T

Flow in fractured porous media occurs in the earth's subsurface, in biological tissues, and in man-made materials. Fractures have a dominating influence on flow processes, and the last decade has seen an extensive development of models and numerical methods that explicitly account for their presence. To support these developments, four benchmark cases for single-phase flow in three-dimensional fractured porous media are presented. The cases are specifically designed to test the methods' capabilities in handling various complexities common to the geometrical structures of fracture networks. Based on an open call for participation, results obtained with 17 numerical methods were collected. This paper presents the underlying mathematical model, an overview of the features of the participating numerical methods, and their performance in solving the benchmark cases.

1. Introduction

Flow in fractured porous media is characterized by an interaction between the fractures and the surrounding porous medium, commonly referred to as the matrix. The strong influence of fracture network geometry on flow patterns has motivated the development of mathematical models and numerical methods that explicitly account for the geometry of fractures (Berre et al., 2019). Considering flow both in the fractures and in the surrounding porous medium, these models are based on the conceptual discrete-fracture-matrix (DFM) representation of the fractured porous media.

With the development of a wealth of simulation tools for flow in fractured porous media, a need for verification benchmarks for numerical methods has emerged. To accommodate this need, four research groups working in the field initiated a comparison study, which led to the presentation of a suite of two-dimensional benchmark tests and corresponding results for a range of numerical methods (Flemisch et al., 2018). The methods were probed on test cases featuring known

* Corresponding author.
E-mail address: bernd@iws.uni-stuttgart.de (B. Flemisch).

https://doi.org/10.1016/j.advwatres.2020.103759
Received 17 February 2020; Received in revised form 15 September 2020; Accepted 21 September 2020
Available online 10 November 2020
0309-1708/© 2020 Published by Elsevier Ltd.

difficulties for numerical methods, including fracture intersections and combinations of blocking and conducting fractures. The study exposed the relative strengths and weaknesses between the participating methods, both in terms of accuracy and computational cost. After the publication of the results, these benchmark cases have been widely applied by the scientific community in testing numerical methods and new simulation tools (Arrarás et al., 2019; Budisa and Hu, 2019; Köppel et al., 2019a; 2019b; Odsæter et al., 2019; Schädle et al., 2019).

Based on the reception of the first benchmark study (Flemisch et al., 2018) and the capabilities of three-dimensional modeling in the research community, the next phase in the work on verification benchmarks was launched with a call for participation (Berre et al., 2018). The purpose of this call was to extend the platform of verification benchmarks for numerical methods to three-dimensional problems. In addition, the studies were extended to include simulations of linear tracer transport as a means to highlight additional nuances in the comparison of the calculated flow fields. The present paper discusses the results received as answers to this call.

The paper is organized as follows. In Section 2, an overview of the participation process is given. Section 3 describes the mathematical models for fluid flow and transport in fractured porous media. Section 4 briefly describes the participating numerical methods as well as the discretization of the transport problem. The four test cases are described in Section 5, with each description followed by a presentation and discussion of the corresponding results. Section 6 summarizes the discussion of the results, and Section 7 provides concluding remarks.

2. Benchmark process

The verification benchmark study was laid out as a four-stage process: the development of benchmark cases, a call for participation, collection and synchronization of the results by the participants, and a final discussion and reporting.

The process started with the participants of the first benchmark study (Flemisch et al., 2018) developing four new test cases. These were designed to test the capabilities of numerical methods for DFM representations of flow in three-dimensional fracture networks. The design of each test case was rendered by the "benchmark case designers" listed in the CRediT author statement at the end of the paper. An open call for participation was launched in September 2018 (Berre et al., 2018), followed by a dedicated mini-symposium at the SIAM Conference on Mathematical and Computational Issues in the Geosciences, March 2019, Houston. Researchers interested in participating in the benchmark followed a predefined registration procedure, were approved by the authors issuing the call, and were asked to sign a participation agreement. During this process, applications concerning 15 additional numerical methods were submitted, all of which were approved by the call authors. Finally, the results of 12 of these methods were submitted and included in the study.

The case descriptions presented in the call (Berre et al., 2018) were accompanied by data in the form of geometry descriptions, existing simulation results, and plotting scripts, all available in the Git repository https://git.iws.uni-stuttgart.de/benchmarks/fracture-flow-3d.git. This repository was reused in the fully transparent collection and synchronization phase. During this phase, the results were uploaded and made available to all participants, and recomputations and adjustments were allowed until August 2019. In the fourth phase, all participants contributed to the reporting of the results presented in Section 5. The last two phases were led by assigned "benchmark case coordinators". While access to the Git repository was restricted to the benchmark participants during the phase of collection and comparison of the results, all data have been made publicly available upon submission of this manuscript. In addition to the data and plotting scripts, five Jupyter notebooks are provided, four focusing on reproducing the figures encountered in Section 5, and one for facilitating the comparison of new results.

3. Mathematical models

This section introduces two models for flow and transport in fractured media. First, the flow model is presented in the conventional equi-dimensional setting, allowing a natural introduction to the physical parameters. From this formulation, an appropriate reduction of the equations results in the mixed-dimensional model that forms the focus of this study. Finally, the equi- and mixed-dimensional transport models are presented.

3.1. Equi-dimensional flow model

Consider a steady-state, incompressible, single-phase flow through a porous medium described by Darcy's law. With the imposition of mass conservation, the governing system of equations is given by

$$\begin{aligned} \boldsymbol{u} + \mathbb{K}\nabla h &= 0, \\ \nabla \cdot \boldsymbol{u} &= q, \end{aligned} \quad \text{in } \Lambda. \tag{1a}$$

Here, $\boldsymbol{u}$ denotes the fluid velocity in m/s, $\mathbb{K}$ is hydraulic conductivity measured in m/s, h is hydraulic head measured in m, and q represents a source/sink term measured in 1/s. The domain $\Lambda \subset \mathbb{R}^3$ will be called the equi-dimensional domain. The following boundary conditions on the boundary $\partial\Lambda$ of Λ complete model (1a):

$$\begin{aligned} h &= \overline{h} && \text{on } \partial\Lambda_h, \\ \boldsymbol{u} \cdot \boldsymbol{n} &= \overline{u} && \text{on } \partial\Lambda_u. \end{aligned} \tag{1b}$$

Assume $\partial\Lambda = \partial\Lambda_h \cup \partial\Lambda_u$, $\partial\Lambda_h \cap \partial\Lambda_u = \emptyset$, and $\partial\Lambda_h \neq \emptyset$. $\overline{h}$ is the hydraulic head imposed on the boundary $\partial\Lambda_h$, while $\overline{u}$ is the prescribed Darcy velocity normal to the boundary $\partial\Lambda_u$ with respect to the outer unit normal vector $\boldsymbol{n}$.

By substituting Darcy's law in the mass conservation, the dual problem (1) can be recast in its primal formulation, given by

$$\begin{aligned} -\nabla \cdot \mathbb{K}\nabla h &= q \ \text{ in } \ \Lambda, \\ h &= \overline{h} \ \text{ on } \ \partial\Lambda_h, \\ -\mathbb{K}\nabla h \cdot \boldsymbol{n} &= \overline{u} \ \text{ on } \partial\Lambda_u. \end{aligned} \tag{2}$$

Problems (1) and (2) are equivalent, however, the two formulations (primal and mixed) require different numerical approximation schemes: for instance, while standard FEM can be applied to (2) a mixed approximation scheme is needed for (1). The reader is referred to Chavent and Jaffré (1986) for more details on the formulation, and to Raviart and Thomas (1977), Brezzi and Fortin (1991), Roberts and Thomas (1991), and Ern and Guermond (2004) for an introduction to mixed methods.

Assume that Λ contains several fractures, i.e., thin inclusions in the domain. The fracture walls are assumed to be planar with smooth boundaries. The fractures have two distinguishing features: a) the thickness, measured by the aperture ε, is small compared to the spatial extent of the fracture; and b) the hydraulic conductivity may differ significantly from that of the rest of Λ. The latter implies that the fractures may have a significant impact on the flow in Λ.

In the setting of equi-dimensional flow, we further make the assumption that the principal directions of the local hydraulic conductivity tensor are aligned with the orientation of the fractures. In particular, the hydraulic conductivity in the matrix ($\mathbb{K}_3$), the fractures ($\mathbb{K}_2$), as well as in the intersections between two fractures ($\mathbb{K}_1$) and at the crossings of intersections ($\mathbb{K}_0$) are (3×3)-tensors and allow for the following decompositions:

$$\mathbb{K}_3 = K_3^{eq}, \quad \mathbb{K}_2 = \begin{bmatrix} K_2^{eq} & & 0 \\ & & 0 \\ 0 & 0 & \kappa_2^{eq} \end{bmatrix},$$

$$\mathbb{K}_1 = \begin{bmatrix} K_1^{eq} & 0 & 0 \\ 0 & \kappa_1^{eq} & 0 \\ 0 & 0 & \kappa_1^{eq} \end{bmatrix}, \quad \mathbb{K}_0 = \begin{bmatrix} \kappa_0^{eq} & 0 & 0 \\ 0 & \kappa_0^{eq} & 0 \\ 0 & 0 & \kappa_0^{eq} \end{bmatrix}.$$

Here, K_{d}^{eq} denotes the tangential hydraulic conductivity for $d = 1, \dots, 3$ and is thus given by a symmetric, positive definite $(d \times d)$-tensor. Moreover, κ_d^{eq} represents the normal hydraulic conductivity, given by a positive scalar. Note that the normal bundle of a line in 3D is two-dimensional whereas all three basis vectors of $\mathbb{R}^3$ are normal to an intersection point. The actual meaning of "tangential" and "normal" hydraulic conductivity will be clear in the subsequent part. The superscript *eq* indicates that these quantities are related to the equi-dimensional model. The subscript *d*, on the other hand, indicates that these parameters will be used on *d*-dimensional objects in the reduced model, which the next section derives.

3.2. Mixed-dimensional flow model

The small aperture of the fractures justifies a reduction of dimensionality to a representation where fractures and their intersections are approximated by lower-dimensional objects. For more details on the derivation of mixed-dimensional models for flow in fractured porous media, the reader is referred to Martin et al. (2005), Angot et al. (2009) and to Kumar et al. (2020), Brenner et al. (2018), Ahmed et al. (2017), List et al. (2020) for extensions concerning two-phase and unsaturated flows.

The mixed-dimensional decomposition of Λ is Ω. It contains the three-dimensional domain Ω_3 that represents the (possibly unconnected) matrix, and, furthermore, up to three lower-dimensional, open subdomains, namely, the union of fracture planes Ω_2, their intersection lines Ω_1 and intersection points Ω_0. Individual lower-dimensional features are referred to as $\Omega_{d,i}$ with *d* its dimension and *i* a uniquely assigned counting index. Finally, $\Gamma_d = \Omega_d \cap \partial\Omega_{d+1}$ is the set of *d*-interfaces between neighboring subdomains of codimension one. Each interface $\Gamma_{d,j}$ is endowed with a unit normal vector $\boldsymbol{n}$. To be mathematically precise, $\boldsymbol{n}$ is chosen from the tangent bundle of the higher-dimensional neighbor $\Omega_{d+1,i}$, is normal to $\Gamma_{d,j}$, and is oriented outward with respect to $\Omega_{d+1,i}$.

Remaining consistent with the notation convention above, data and unknowns will also be annotated with a subscript related to the dimension. As a first example, on a *d*-dimensional subdomain $\Omega_{d,i}$, let $\varepsilon_{d,i}$ denote the cross-sectional volume, area, or length of the corresponding physical domain for $d = 0, \dots, 2$, respectively. It has the unit of measure $\mathrm{m}^{3-\mathrm{d}}$ and its definition extends to the three-dimensional bulk as $\varepsilon_3 = 1$. Moreover, a typical length $a_{d,i}$ is defined such that $\varepsilon_{d,i} = a_{d,i}^{3-d}$.

The continuation of this subsection presents the reduced model associated with (1) in the two-dimensional fractures Ω_2 followed by its generalization for all $d = 0, \dots, 3$.

3.2.1. Flow in fractures

To present the flow model, the derivation done in Martin et al. (2005) and Boon et al. (2018) has been considered. The variables in this formulation are the velocity $\boldsymbol{u}_3 = \boldsymbol{u}$ and hydraulic head $h_3 = h$ in the rock matrix Ω_3, as well as the integrated tangential velocity $\boldsymbol{u}_2$ and average hydraulic head h_2 in the fracture. These are given pointwise for $x \in \Omega_2$ by

$$\boldsymbol{u}_2(x) = \int_{\varepsilon_2(x)} \boldsymbol{u}_\parallel \quad \text{and} \quad h_2(x) = \frac{1}{\varepsilon_2(x)} \int_{\varepsilon_2(x)} h.$$

Here, $\boldsymbol{u}_\parallel$ denotes the components of $\boldsymbol{u}$ tangential to Ω_2. The integrals are computed in the normal direction of the fracture, and thus, the corresponding units of measurement are m^3/s and m for $\boldsymbol{u}_2$ and h_2, respectively.

Averaging and integrating, respectively, over the direction normal to the fractures derives the reduced Darcy's law and mass balance equation. Recall that the vector $\boldsymbol{n}$ here refers to the normal unit vector oriented outward from Ω_3. We have

$$\begin{aligned} \frac{1}{\varepsilon_2}\boldsymbol{u}_2 + K_2^{eq}\nabla_2 h_2 &= 0 \\ \nabla_2 \cdot \boldsymbol{u}_2 - [\![\boldsymbol{u}_3 \cdot \boldsymbol{n}]\!] &= q_2 \end{aligned} \quad \text{in } \Omega_2, \tag{3a}$$

where ∇_2 is the del-operator in the tangential directions and q_2 is the integrated source term, i.e., $q_2(s) = \int_{\varepsilon_2(s)} q$.

Note the assumption that K_2^{eq} is constant in the direction normal to Ω_2. The jump operator is defined as $[\![\boldsymbol{u}_3 \cdot \boldsymbol{n}]\!]|_{\Omega_d} = \sum(\boldsymbol{u}_3 \cdot \boldsymbol{n}|_{\Gamma_2})$, thus representing the mass exchange between fracture and matrix. In particular, for each subdomain $\Omega_{2,i} \subseteq \Omega_2$, all flux contributions are summed over sections of Γ_2 that coincide geometrically with $\Omega_{2,i}$. These fluxes are assumed to satisfy the following Darcy-type law given by a finite difference between the hydraulic head in Ω_2 and on $\partial\Omega_3$:

$$\boldsymbol{u}_3 \cdot \boldsymbol{n} + \kappa_2^{eq}\frac{2}{a_d}(h_2 - h_3) = 0 \quad \text{on } \Gamma_2. \tag{3b}$$

3.2.2. Generalization to intersections and complete model

The following generalizes the equations described above to domains of all dimensions, thus including the intersection lines and points. For that purpose, the integrated velocity $\boldsymbol{u}_d$ for $d = 1$ and average hydraulic head h_d with $d = 0, 1$ are introduced, and given pointwise for $x \in \Omega_d$ by

$$\boldsymbol{u}_1(x) = \int_{\varepsilon_1(x)} \boldsymbol{u}_\parallel \quad \text{and} \quad h_d(x) = \frac{1}{\varepsilon_d(x)} \int_{\varepsilon_d(x)} h, \text{ for } d = 0, 1.$$

Again, $\boldsymbol{u}_\parallel$ denotes the components of $\boldsymbol{u}$ tangential to Ω_1. The corresponding units of measurement are m^2/s and m for $\boldsymbol{u}_1$ and h_d, respectively. The analogs of (3a) on these lower-dimensional manifolds are then given by

$$\begin{aligned} \frac{1}{\varepsilon_1}\mathbf{u}_1 + K_1^{eq}\nabla_1 h_1 &= 0 \\ \nabla_1 \cdot \mathbf{u}_1 - [\![\mathbf{u}_2 \cdot \mathbf{n}]\!] &= q_1 \quad \text{in } \Omega_1, \\ -[\![\mathbf{u}_1 \cdot \mathbf{n}]\!] &= q_0 \quad \text{in } \Omega_0. \end{aligned} \tag{4}$$

Here, ∇_1 denotes the del-operator, i.e., the derivative, in Ω_1. For each $\Omega_{d,i}$, the linear jump operator $[\![\cdot]\!]$ is naturally generalized to $[\![\boldsymbol{u}_{d+1} \cdot \boldsymbol{n}]\!]|_{\Omega_{d,i}} = \sum(\boldsymbol{u}_{d+1} \cdot \boldsymbol{n}|_{\Gamma_{d,j}})$, where all flux contributions are summed over sections $\Gamma_{d,j} \subseteq \Gamma_d$ that coincide geometrically with $\Omega_{d,i}$. Finally, q_1 and q_0 correspond to the integrated source terms in the intersection lines and points, respectively.

Due to our choice of defining $\boldsymbol{u}_d$ as the integrated velocity, a scaling with ε_{d+1} appears in the equation governing the flux across Γ_d:

$$\frac{1}{\epsilon_{d+1}}\boldsymbol{u}_{d+1} \cdot \boldsymbol{n} + \kappa_d^{eq}\frac{2}{a_d}(h_d - h_{d+1}) = 0 \quad \text{on } \Gamma_d,\ d = 0, 1. \tag{5}$$

Recalling that $\epsilon_3 = 1$, it now follows that the effective tangential and normal hydraulic conductivities are given by:

$$K_{\mathrm{d}} = \varepsilon_d K_{\mathrm{d}}^{eq}, \qquad \text{in } \Omega_d,\ d = 1, \dots, 3 \tag{6a}$$

$$\kappa_d = \varepsilon_{d+1}\frac{2}{a_d}\kappa_d^{eq}, \qquad \text{on } \Gamma_d,\ d = 0, \dots, 2. \tag{6b}$$

From these definitions, it is clear that the units of K_{d} and κ_d are $\mathrm{m}^{4-\mathrm{d}}/\mathrm{s}$ and $\mathrm{m}^{2-\mathrm{d}}/\mathrm{s}$, respectively.

Collecting the above equations gives the generalization of system (3) to subdomains of all dimensions. The system consists of Darcy's law in both tangential and normal directions followed by the mass conservation equations:

$$\boldsymbol{u}_d + K_{\mathrm{d}}\nabla_d h_d = 0, \qquad \text{in } \Omega_d,\ d = 1, \dots, 3, \tag{7a}$$

$$\boldsymbol{u}_{d+1} \cdot \boldsymbol{n} + \kappa_d(h_d - h_{d+1}) = 0, \quad \text{on } \Gamma_d,\ d = 0, \dots, 2, \tag{7b}$$

$$\nabla_d \cdot \boldsymbol{u}_3 = q_3, \qquad \text{in } \Omega_3, \tag{7c}$$

$$\nabla_d \cdot \boldsymbol{u}_d - [\![\boldsymbol{u}_{d+1} \cdot \boldsymbol{n}]\!] = q_d, \qquad \text{in } \Omega_d,\ d = 1, 2, \tag{7d}$$

$$-[\![\boldsymbol{u}_1 \cdot \boldsymbol{n}]\!] = q_0, \qquad \text{in } \Omega_0. \tag{7e}$$

The source term is given by q_3 for the rock matrix and $q_d(x) = \int_{\varepsilon_d(x)} q$ measured in $\mathrm{m}^{3-\mathrm{d}}/\mathrm{s}$.

System (7) is then compactly described by:

$$\boldsymbol{u}_d + K_{\mathrm{d}} \nabla_d h_d = 0, \qquad \text{in } \Omega_d,\ d = 1, \dots, 3, \tag{8a}$$

$$\boldsymbol{u}_{d+1} \cdot \boldsymbol{n} + \kappa_d (h_d - h_{d+1}) = 0, \quad \text{on } \Gamma_d,\ d = 0, \dots, 2, \tag{8b}$$

$$\nabla_d \cdot \boldsymbol{u}_d - [\![\boldsymbol{u}_{d+1} \cdot \boldsymbol{n}]\!] = q_d, \qquad \text{in } \Omega_d,\ d = 0, \dots, 3, \tag{8c}$$

in which the nonphysical $\boldsymbol{u}_4$ and $\boldsymbol{u}_0$ are understood as zero. The boundary conditions are inherited from the equidimensional model with the addition of a no-flux condition at embedded fracture endings:

$$h_d = \overline{h} \qquad \text{on } \partial\Omega_d \cap \partial\Lambda_h,\ d = 0, \dots, 3, \tag{9a}$$

$$\boldsymbol{u}_d \cdot \boldsymbol{n} = \varepsilon_d \overline{u} \qquad \text{on } \partial\Omega_d \cap \partial\Lambda_u,\ d = 1, \dots, 3, \tag{9b}$$

$$\boldsymbol{u}_d \cdot \boldsymbol{n} = 0 \qquad \text{on } \partial\Omega_d \backslash (\Gamma_{d-1} \cup \partial\Lambda),\ d = 1, \dots, 3. \tag{9c}$$

Finally, this section presents the primal formulation of the mixed-dimensional fracture flow model. Analogous to (2), this formulation is derived by substituting Darcy's laws (8a) and (8b) into the conservation Eq. (8c):

$$-\nabla_d \cdot K_{\mathrm{d}} \nabla_d h_d + [\![\kappa_d (h_d - h_{d+1})]\!] = q_d, \text{ in } \Omega_d,\ d = 0, \dots, 3. \tag{10}$$

Again, the divergence term is interpreted as zero if $d = 0$ and the jump term as zero if $d = 3$. The boundary conditions are given by

$$h_d = \overline{h} \qquad \text{on } \partial\Omega_d \cap \partial\Lambda_h,\ d = 0, \dots, 3, \tag{11a}$$

$$-K_{\mathrm{d}} \nabla_d h_d \cdot \boldsymbol{n} = \varepsilon_d \overline{u} \qquad \text{on } \partial\Omega_d \cap \partial\Lambda_u,\ d = 1, \dots, 3, \tag{11b}$$

$$-K_{\mathrm{d}} \nabla_d h_d \cdot \boldsymbol{n} = 0 \qquad \text{on } \partial\Omega_d \backslash (\Gamma_{d-1} \cup \partial\Lambda),\ d = 1, \dots, 3. \tag{11c}$$

Many discretization schemes presented in this study ignore flow in the one-dimensional fracture intersections and zero-dimensional intersections thereof. Although these correspond to discretizing a simpler model, this is perfectly in line with the proposed study.

3.3. Equi-dimensional transport model

A scalar quantity c with the unit of measure m^{-3} is transported through the porous medium subject to the velocity field resulting from the flow model presented in the previous sections. The purely advective transport of c is described by the conservation equation:

$$\phi \frac{\partial c}{\partial t} + \nabla \cdot (c\boldsymbol{u}) = q_c \quad \text{in } \Lambda, \tag{12}$$

where ϕ is the porosity of the medium and q_c is a source/sink term for c given in $\mathrm{m}^{-3}/\mathrm{s}$. Boundary segments where inflow occurs have Dirichlet boundary conditions, i.e.,

$$c|_{\partial\Lambda_c} = \overline{c} \quad \text{on } \partial\Lambda_c, \quad \partial\Lambda_c = \{x \in \partial\Lambda : \ \boldsymbol{u} \cdot \boldsymbol{n} < 0\}, \tag{13}$$

with $\overline{c}$ being the value for c prescribed on the boundary $\partial\Lambda_c$.

3.4. Mixed-dimensional transport model

Analogous to Section 3.2, the average value for c is chosen as the primary variable, which is defined as $c_3 = c$ in Ω_3 and for the lower dimensional objects (with $d \leq 2$) as

$$c_d(s) = \frac{1}{\varepsilon_d(s)} \int_{\varepsilon_d(s)} c.$$

Following the derivation of the mixed-dimensional flow model presented in Section 3.2, the resulting mixed-dimensional transport model reads as:

$$\varepsilon_d \phi_d \frac{\partial c_d}{\partial t} + \nabla_d \cdot \left(c_d \boldsymbol{u}_d\right) - [\![\tilde{c}_{d+1} \left(\boldsymbol{u}_{d+1} \cdot \boldsymbol{n}\right)]\!] = q_{c,d} \quad \text{in } \Omega_d, \quad d = 0, \dots, 3. \tag{14}$$

Note that for $d = 0$, the divergence term is void and for $d = 3$ the contribution of the jump operator is set to null. Here, the porosity is simply $\phi_d = \phi^{eq}$ and $\tilde{c}_{d+1}$ is evaluated on the basis of a first-order upwind scheme, i.e.,

$$\tilde{c}_{d+1} = \begin{cases} c_{d+1} & \text{if} \quad \boldsymbol{u}_{d+1} \cdot \boldsymbol{n}|_{\Gamma_d} > 0 \\ c_d & \text{if} \quad \boldsymbol{u}_{d+1} \cdot \boldsymbol{n}|_{\Gamma_d} < 0. \end{cases} \tag{15}$$

As in the flow model, the jump operator represents the sum of the fluxes over all contributions defined on sections of Γ_d that coincide geometrically with $\Omega_{d,i}$.

4. Participating discretization methods

The intent of this benchmark study is to quantitatively evaluate different discretization schemes for the mixed-dimensional flow models (8)-(11). The modeling error resulting from averaging the underlying equi-dimensional models is deliberately disregarded. In the sense of this study, the solution to be approximated by the participating methods is the solution to the corresponding mixed-dimensional model, not the equi-dimensional one. For a detailed benchmark study taking into account the modeling error from averaging, see Flemisch et al. (2018). As a means of evaluating a discrete solution, the velocities were inserted into a standard cell-centered, first-order upwind scheme for the transport Eq. (14). The temporal discretization is given by the implicit Euler method with a fixed time-step prescribed for each test case. The main properties of the discretization methods covered by the benchmark are summarized in Tables 1 and 2, which also contain references for further details. The majority of the methods followed the mixed-dimensional flow model and the specified transport discretization, with the following exceptions:

The schemes `NCU_TW-Hybrid_FEM` and `DTU-FEM_COMSOL` describe the flow along the fractures by additional terms defined on the fracture surfaces. This effectively adds connectivity between the degrees of freedom located on fractures without introducing additional degrees of freedom. This means that these schemes do not solve the mass balances (8c) for $d < 3$. Moreover, this approach implies continuity of the hydraulic head across the fractures and therefore replaces the coupling condition (8b). Other schemes participating in this study also assume continuity of the hydraulic head across the fractures, and a complete overview is given in Table 2.

The scheme `UNIL_USI-FE_AMR_AFC` is an equi-dimensional approach, meaning that the fractures, their intersections, and intersections of intersections are discretized with three-dimensional elements using locally refined grids. Therefore, the lower-dimensional mass balances (8c) for $d < 3$ and the coupling conditions (8b) are not relevant for this scheme.

Finally, the schemes `ETHZ_USI-FEM_LM` and `UNIL_USI-FE_AMR_AFC` do not use a first-order upwind scheme but apply an algebraic flux correction technique for the stabilization of a finite element discretization of the transport model (Kuzmin et al., 2012). Such stabilization techniques provide a similar discretization as the given upwind scheme.

5. Benchmark cases and results

This section presents the benchmark cases and compares the submitted results. For each case, the hydraulic head and tracer concentration are compared using several predefined macroscopic metrics. In Section 5.1, a benchmark case containing a single fracture problem is considered. Section 5.2 presents a benchmark based on a synthetic network composed of nine regularly arranged fractures. The benchmark case in Section 5.3 considers the geometrically challenging case of almost intersecting fractures, fractures with small intersections, and other features that a fracture network may exhibit. Finally, Section 5.4 studies a case with 52 fractures selected from a real network.

Table 1
Names, acronyms, references and test cases covered for all participating discretization methods.

Acronym	References	Open source code	Run scripts	Test cases
		Two-point flux approximation		
UiB-TPFA	Keilegavlen et al. (2019) and Nordbotten et al. (2019)	✓[a]	✓[b]	1–4
		Multi-point flux approximation		
UiB-MPFA	Keilegavlen et al. (2019) and Nordbotten et al. (2019)	✓[a]	✓[b]	1–4
		Lowest order mixed virtual element method		
UiB-MVEM	Keilegavlen et al. (2019) and Nordbotten et al. (2019)	✓[a]	✓[b]	1–4
		Lowest order Raviart-Thomas mixed finite elements		
UiB-RT0	Keilegavlen et al. (2019), Nordbotten et al. (2019), and Boon et al. (2018)	✓[a]	✓[b]	1–4
		Multi-point flux approximation		
USTUTT-MPFA	Koch et al. (2020)	✓[c]	✓[d]	1–4
		Two-point flux approximation		
USTUTT-TPFA_Circ	Koch et al. (2020)	✓[c]	✓[d]	1–4
		Mimetic Finite Differences		
LANL-MFD	Lipnikov et al. (2014)	✓[e]	×	1–4
		Hybrid finite element method		
NCU_TW-Hybrid_FEM	Lee and Ni (2015) and Lee et al. (2019)	×	×	1
		Vertex Approximate Gradient continuous hydraulic head		
UNICE_UNIGE-VAG_Cont	Brenner et al. (2016a)	×	×	1–4
		Hybrid Finite Volumes continuous hydraulic head		
UNICE_UNIGE-HFV_Cont	Brenner et al. (2016a)	×	×	1–4
		Vertex Approximate Gradient discontinuous hydraulic head		
UNICE_UNIGE-VAG_Disc	Brenner et al. (2016b)	×	×	1–4
		Hybrid Finite Volumes discontinuous hydraulic head		
UNICE_UNIGE-HFV_Disc	Brenner et al. (2016b)	×	×	1–4
		Lagrange multiplier - L2-projection finite elements		
ETHZ_USI-FEM_LM	Schädle et al. (2019), Köppel et al. (2019b), and Krause and Zulian (2016)	✓Zulian et al. (2016)	×	1–4
		Hybrid H(div)		
UNICAMP-Hybrid_Hdiv	Devloo et al. (2019) and Durán et al. (2019)	✓[f]	✓[f]	1–4
		Flux-corrected finite element method and adaptive mesh refinement		
UNIL_USI-FE_AMR_AFC	Favino et al. (2020) and Kuzmin et al. (2012)	✓Zulian et al. (2016)	×	1–3
		Embedded discrete fracture method		
INM-EDFM	Nikitin and Yanbarisov (2020)	×	×	1,3
		First-order Lagrangian finite elements (COMSOL)		
DTU-FEM_COMSOL	COMSOL (2019)[g]	×	✓Berre et al. (2020)	1–4

[a] https://github.com/pmgbergen/porepy. 2019.
[b] https://github.com/pmgbergen/arXiv_1809_06926. 2019.
[c] https://git.iws.uni-stuttgart.de/dumux-repositories/dumux. 2019.
[d] https://git.iws.uni-stuttgart.de/dumux-pub/berre2020. 2020.
[e] https://github.com/amanzi. 2019.
[f] https://github.com/labmec/HDiv/tree/master/HDiv_Benchmarks. 2019.
[g] https://www.comsol.com/release/5.4. 2019.

The reasoning behind the design of the four cases is to isolate typical challenges encountered in practice by means of dedicated synthetic scenarios. The focus is always on the behavior of the discretization methods in the presence of fractures. While considering a full geologically relevant outcrop model would be interesting, adding such a case would make it impossible to track down the reasons for differences in the results and is therefore out of scope for this study. For similar reasons, investigating strong local heterogeneities in the matrix itself as well as upscaling approaches are excluded.

5.1. *Case 1: Single fracture*

5.1.1. *Description*

Fig. 1 illustrates the first benchmark case, with a geometry that is slightly modified from works Zielke et al. (1991) and Barlag et al. (1998). The domain Ω is a cube-shaped region (0m, 100m) × (0m, 100m) × (0m, 100m) which is crossed by a planar fracture, Ω_2, with a thickness of 0.01m. The matrix domain consists of subdomains $\Omega_{3,1}$ above the fracture and $\Omega_{3,2}$ and $\Omega_{3,3}$ below. The subdomain $\Omega_{3,3}$ represents a heterogeneity within the rock matrix. Inflow

Table 2
Numerical properties for the discretization methods. An entry in the column "conforming" can be "fully" if each fracture element needs to coincide with a facet shared by two neighboring matrix elements, "geometrically" if each fracture needs to be a union of element facets from each of the two neighboring matrix subdomain meshes, or "none" if fracture and matrix meshes can be completely independent of each other.

Acronym	Degrees of freedom	Local mass conservation	Allows h discontinuity	Conformity	Subdomain dimensions
UiB-TPFA	h (elem), λ (mortar flux)	✓	✓	Geometrically	0–3
UiB-MPFA	h (elem), λ (mortar flux)	✓	✓	Geometrically	0–3
UiB-MVEM	h (elem), $\boldsymbol{u}$ (faces), λ (mortar flux)	✓	✓	Geometrically	0–3
UiB-RTO	h (elem), $\boldsymbol{u}$ (faces), λ (mortar flux)	✓	✓	Geometrically	0–3
USTUTT-MPFA	h (elem)	✓	✓	Fully	2–3
USTUTT-TPFA_Circ	h (elem)	✓	✓	Fully	2–3
LANL-MFD	h (faces)	✓	✓	Fully	2–3
NCU_TW-Hybrid_FEM	h, $\boldsymbol{u}$ (nodes)	✓	×	Fully	2–3
UNICE_UNIGE-VAG_Cont	h (nodes), (fracture faces)	✓	×	Conforming	2–3
UNICE_UNIGE-VAG_Disc	h (nodes), (fracture faces)	✓	✓	Conforming	2–3
UNICE_UNIGE-HFV_Cont	h (faces), (fracture edges)	✓	×	Conforming	2–3
UNICE_UNIGE-HFV_Disc	h (faces), (fracture edges)	✓	✓	Conforming	2–3
ETHZ_USI-FEM_LM	h (nodes) λ (nodes)	×	×	None	2–3
UNICAMP-Hybrid_Hdiv	h, $\boldsymbol{u}$ (elem), λ (faces)	✓	✓	Geometrically	0–3
UNIL_USI-FE_AMR_AFC	h (nodes)	✓	×	Not applicable	equi-dim.
INM-EDFM	h (elem)	✓	×	None	2–3
DTU-FEM_COMSOL	h (nodes)	✓	×	Fully	2–3

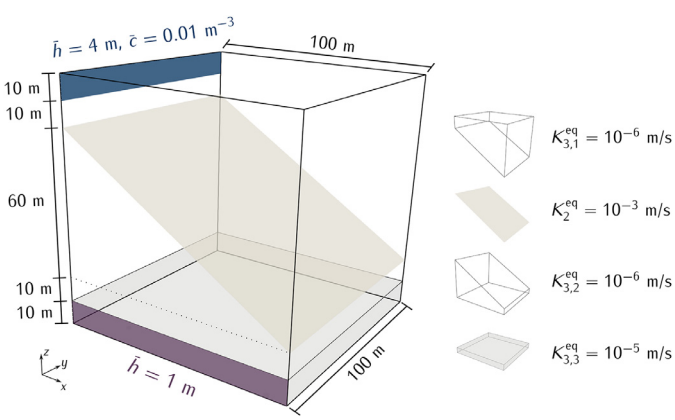

Fig. 1. Conceptual model and geometrical description of the domain for Case 1 of Section 5.1. Inlet and outlet part of the boundary are indicated in blue and purple, respectively. (For interpretation of the references to color in this figure legend, the reader is referred to the web version of this article.)

into the system occurs through a narrow band defined by {0m} × (0m, 100m) × (90m, 100m). Similarly, the outlet is a narrow band defined by (0m, 100m) × {0m} × (0m, 10m).

At the inlet and outlet bands, the hydraulic head is set to $h_{in} = 4$m and $h_{out} = 1$m respectively, and $c_{in} = 0.01\text{m}^{-3}$ is set at the inlet for the transport problem. All remaining parts of the boundary are assigned no-flow conditions. The parameters for conductivity, porosity, and aperture are listed in Table 3 together with the overall simulation time and time-step size.

5.1.2. Results

Three different simulations were carried out with approximately 1k, 10k and 100k cells for the 3d domain. The precise number of cells and degrees of freedom for each method are listed in Table A.7 and will be discussed in Section 5.1.2.7. The basis for comparison of the methods is computed pressure head and concentration, plotted along prescribed lines. The first comparison, represented in Section 5.1.2.1, depicts the hydraulic head along a line crossing the 3d matrix domain, while the solutions reported in 5.1.2.2 and 5.1.2.3 visualize the matrix and fracture concentration along lines at the final simulation time. The purpose of these three plots is to visualize the spread of the solutions, in particular its reduction upon grid refinement. To this end, for a quantity such as the concentration c let $c^{[i]}$ denote the i-th percentile of the provided numerical solutions. The quantification of the spread of the solutions along a given line ξ is based on the following measures:

$$\sigma_c^{[i]} = \frac{c^{[i]} - c^{\text{ref}}}{\bar{c}^{\text{ref}}}, \qquad \sigma_c = \frac{\int_\xi \left(c^{[90]} - c^{[10]}\right) \mathrm{d}x}{\int_\xi c^{\text{ref}} \, \mathrm{d}x}. \tag{16}$$

Here, c^{ref} is the reference solution and $\bar{c}^{\text{ref}}$ is its average over ξ. We note that σ_c is equal to the mean of $(\sigma_c^{[90]} - \sigma_c^{[10]})$ over ξ.

Plots in Section 5.1.2.4 and 5.1.2.5 depict integrated matrix and fracture concentrations over time, respectively. Finally, Section 5.1.2.6 presents comparison of concentration fluxes across the outlet over time.

Table 3
Parameters used in Case 1 of Section 5.1.

Matrix hydraulic conductivity $K_{3,1}$, $K_{3,2}$	$1 \times 10^{-6}\boldsymbol{I}$	m/s
Matrix hydraulic conductivity $K_{3,3}$	$1 \times 10^{-5}\boldsymbol{I}$	m/s
Fracture effective tangential hydraulic conductivity K_2	$1 \times 10^{-3}\boldsymbol{I}$	m^2/s
Fracture effective normal hydraulic conductivity κ_2	20	1/s
Matrix porosity $\phi_{3,1}$, $\phi_{3,2}$	2×10^{-1}	
Matrix porosity $\phi_{3,3}$	$2.5 \times 10{-}1$	
Fracture porosity ϕ_2	4×10^{-1}	
Fracture cross-sectional length ϵ_2	1×10^{-2}	m
Total simulation time	1×10^9	s
Time-step Δt	1×10^7	s

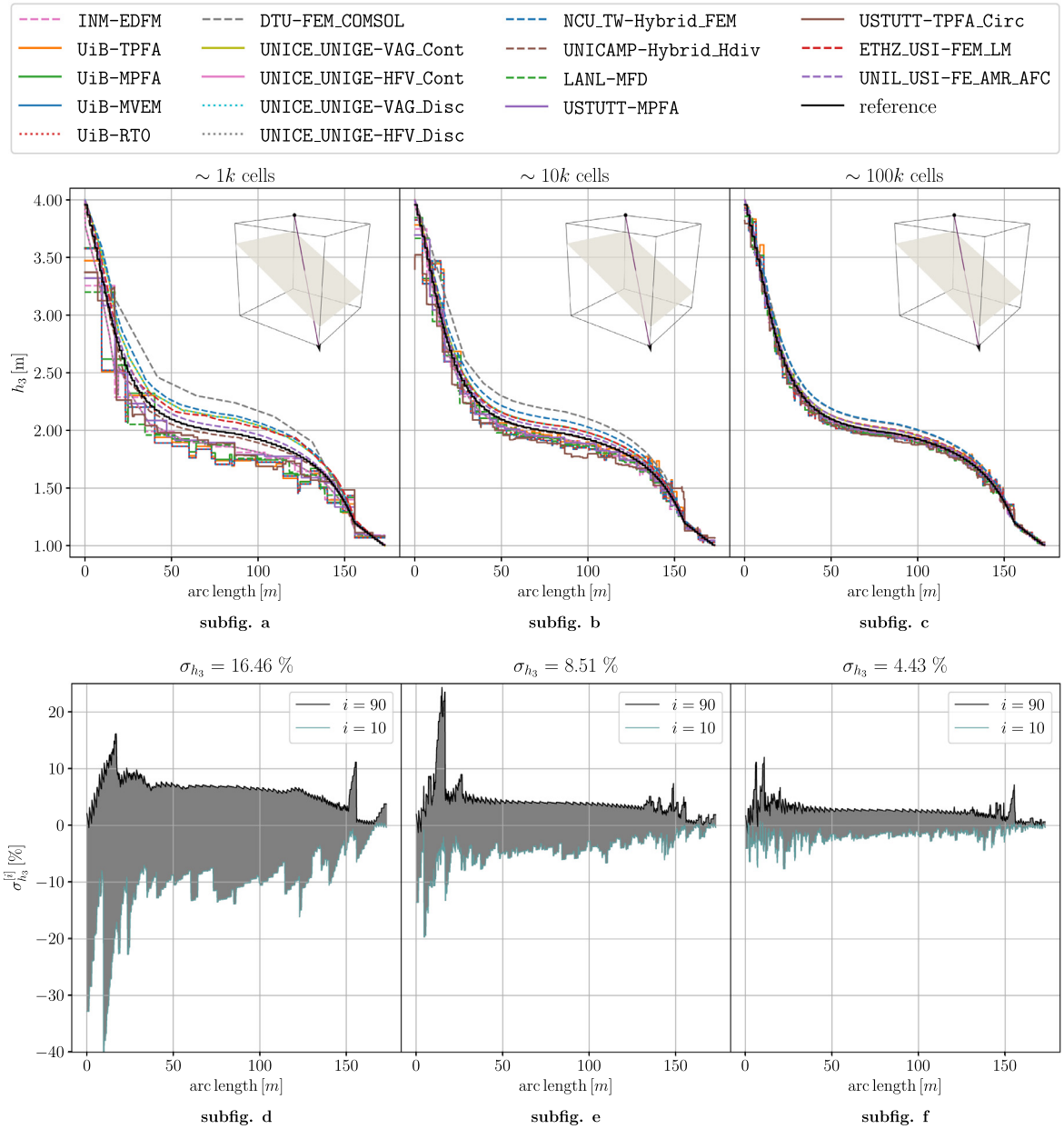

Fig. 2. Case 1 of Section 5.1. On the top, the hydraulic head h_3 in the matrix over the line (0m, 100m, 100m) - (100m, 0m, 0m) for three refinements (coarse to fine). The reference was computed with the `USTUTT-MPFA` scheme on a refined grid with 1,991,176 cells Gläser (2020). On the bottom, the deviations $\sigma_{h_3}^{[90]}$ and $\sigma_{h_3}^{[10]}$ from the reference solution are illustrated, as defined in (16). Results of Section 5.1.2.1.

5.1.2.1. Hydraulic Head Over Line. Fig. 2 depicts the hydraulic head h_3 in the matrix along the line $(0\text{m}, 100\text{m}, 100\text{m}) - (100\text{m}, 0\text{m}, 0\text{m})$. Each plot corresponds to one of the three refinement levels.

At the coarsest level of around 1000 cells, all methods already show reasonable agreement. As expected, differences between the methods as well as to the reference solution decrease with increasing refinement level. Two classes of methods can be distinguished in these plots. First, the methods that use cellwise constant values exhibit staircase-like patterns. On the other hand, methods using nodal values are interpolated within each cell and yield a smoother appearance.

To quantify the differences between the participating methods and their convergence behavior over all refinement levels, the spread of the associated data sets is evaluated as outlined above and visualized in the bottom row of pictures. The number σ_{h_3} in each picture's title is calculated by (16) and quantifies the observed convergence behavior. The spikes in the local differences obviously result from the cellwise constant solution values. While a possible post-processing procedure could have reduced these differences, it would obscure the differences in the raw result data and is therefore excluded deliberately.

5.1.2.2. Matrix Concentration Over Line. The pictures at the top of Fig. 3 illustrate the concentration c_3 in the matrix at the final simulation time along the line $(0\text{m}, 100\text{m}, 100\text{m}) - (100\text{m}, 0\text{m}, 0\text{m})$, again for the different refinement levels. The behavior is similar to that in 5.1.2.1 in the sense that the differences between most of the methods decrease with increasing refinement level. However, two methods show more pronounced deviations from the rest: `ETHZ_USI-FEM_LM` exhibits oscillations that can be attributed to the fact that the employed algebraic flux correction stabilization scheme does not suppress all spurious oscillations. The `NCU_TW-Hybrid_FEM` does not capture the curve behavior at all. The obviously larger spread in the results is visualized more explicitly in the bottom row of Fig. 3, showing much slower convergence compared to

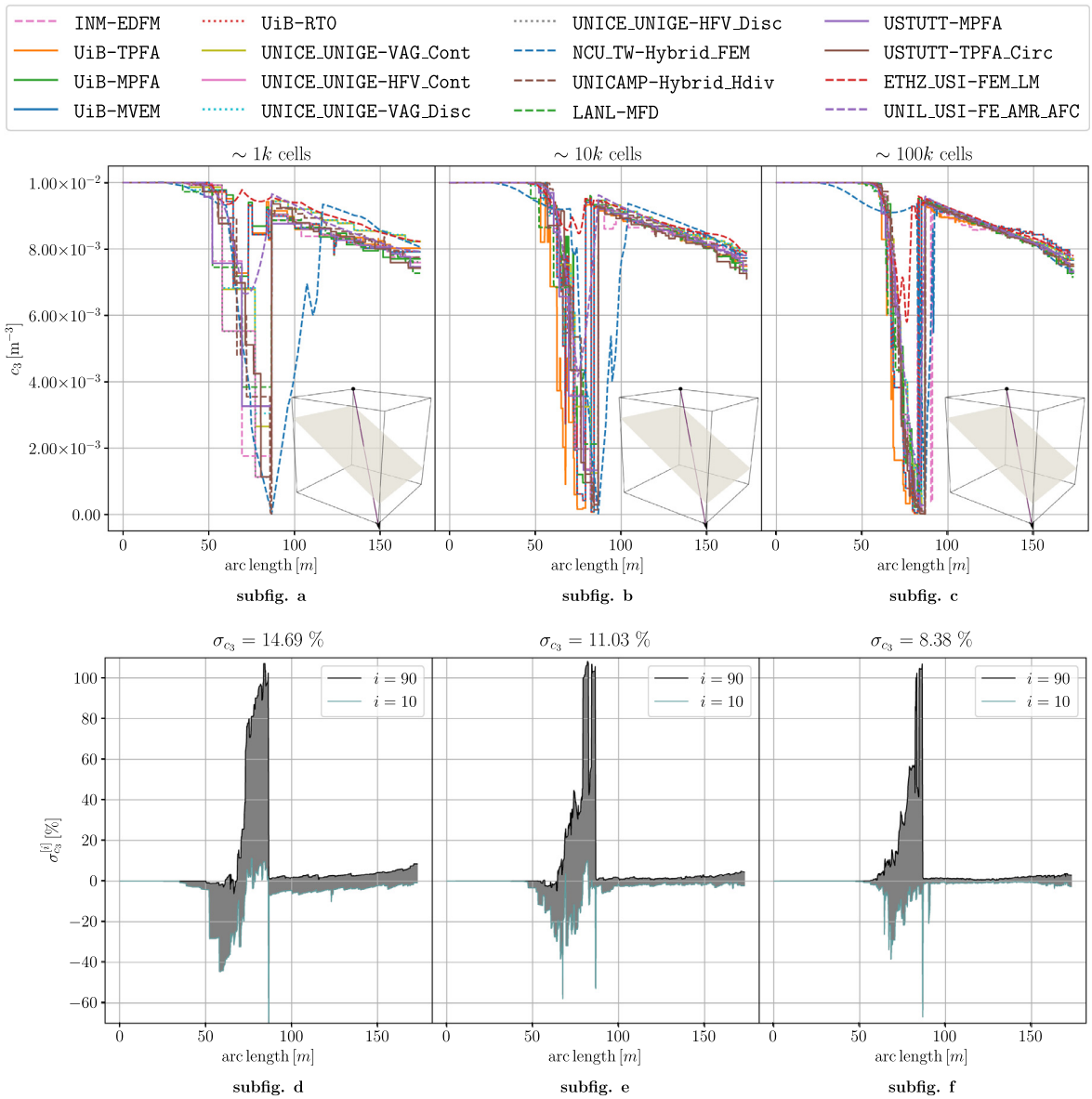

Fig. 3. Case 1 of Section 5.1. On the top, concentration c_3 in the matrix, at the final simulation time, along the line (0m, 100m, 100m) - (100m, 0m, 0m) for three refinements (coarse to fine). On the bottom, the deviations $\sigma_{c_3}^{[90]}$ and $\sigma_{c_3}^{[10]}$ from the median $c_3^{\text{ref}} = c_3^{[50]}$ of the solutions on the finest grid are illustrated. Results of Section 5.1.2.2.

Section 5.1.2.1. The magnitude of the local spread is clearly influenced by the presence of the fracture.

5.1.2.3. Fracture Concentration Over Line. Fig. 4 shows the concentration c_2 within the fracture at the final simulation time along the line $(0\text{m}, 100\text{m}, 80\text{m}) - (100\text{m}, 0\text{m}, 20\text{m})$.

Again, almost all methods appear to converge with increasing refinement. NCU_TW-Hybrid_FEM exhibit the largest deviations over all refinement levels. Close to the outlet boundary, ETHZ_USI-FEM_LM yields rather different values than the rest of the methods, but it clearly approaches the other methods with increasing refinement. Minor deviations close to the outlet can also be observed for INM-EDFM, UiB-RTO and UiB-MVEM which become more pronounced for higher refinement levels. Moreover, UiB-TPFA obviously underestimates the concentration in the medium observed arc length for the finest grids. Looking at the bottom row of Fig. 4, the convergence behavior of the spread is better than that of the matrix concentration reported in Section 5.1.2.2, yet worse than for the matrix hydraulic head in Section 5.1.2.1. Since the inflow boundary with an associated Dirichlet boundary condition is located at the beginning of the line, the spread is considerably lower there and increases over the arc length, i.e., the distance to this boundary.

5.1.2.4. Integrated Matrix Concentration Over Time. Unlike the first three plots in 5.1.2.1–5.1.2.3, Fig. 5 illustrates an integrated quantity over time, namely, the integrated matrix concentration $\int_{\Omega_{3,3}} \phi_3 c_3 \, \mathrm{d}x$. Correspondingly, all curves appear much smoother than above. Over the three refinement levels, most methods again exhibit decreasing differences between each other. Remarkably, the UiB-TPFA shows a pronounced underestimation that increases over time. This can be explained by the inconsistency of the employed two-point flux approximation on the tetrahedral grids. Additionally, the NCU_TW-Hybrid_FEM and ETHZ_USI-FEM_LM again exhibit larger differences.

5.1.2.5. Integrated Fracture Concentration Over Time. Analogously, the integrated fracture concentration $\int_{\Omega_2} \epsilon_2 \phi_2 c_2 \, \mathrm{d}x$ for each time-step is visualized in Fig. 6. The behavior of the curves is generally different from that reported in Section 5.1.2.4, as the fracture fills up completely before the final simulation time. Here, the UiB-TPFA is in

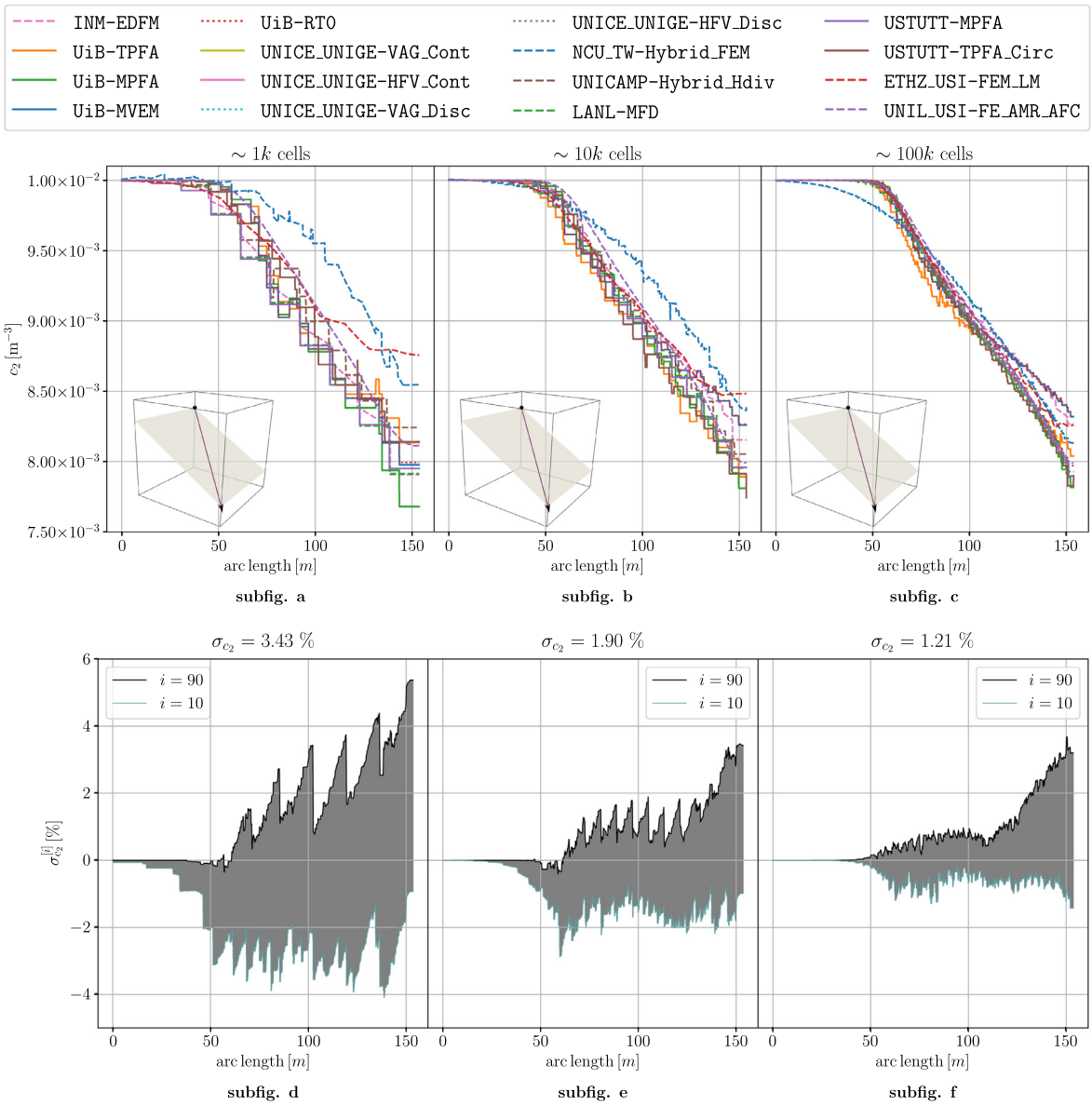

Fig. 4. Case 1 of Section 5.1. On the top, concentration c_2 within the fracture, at the final simulation time, along the line $(0\text{m}, 100\text{m}, 80\text{m}) - (100\text{m}, 0\text{m}, 20\text{m})$ for three refinements (coarse to fine). On the bottom, the deviations $\sigma_{c_2}^{[90]}$ and $\sigma_{c_2}^{[10]}$ are illustrated, as defined in (16). Here, the median $c_2^{[50]}$ of the solutions on the finest grid is used as the reference solution c_2^{ref}. Results of Section 5.1.2.3.

line with the other methods whereas the NCU_TW-Hybrid_FEM and ETHZ_USI-FEM_LM both deviate from the majority.

5.1.2.6. Concentration Flux Across the Outlet Over Time. Finally, Fig. 7 depicts the integrated concentration flux across the outlet boundary over time. Compared to the results in Section 5.1.2.5, the agreement between the methods appears to be poorer. In particular, the two-point flux approximation of the UiB-TPFA results in an underestimation similar to that reported in 5.1.2.4. Again, ETHZ_USI-FEM_LM and NCU_TW-Hybrid_FEM yield considerably different results at all refinement levels.

5.1.2.7. Computational Cost. Indicators for the computational costs associated with the different methods are presented in Table A.7. Most methods satisfy the prescribed numbers of elements. The most notable exception is given by the NCU_TW-Hybrid_FEM, where six to ten times as many tetrahedral elements have been employed, to compensate for the fact that the degrees of freedom are associated with the vertices. The number of vertices are in line with the prescribed cell numbers. The relations of the number of degrees of freedom to the number of cells vary considerably between the different schemes, reflecting the characteristics from Table 2. The lowest of such numbers are for the purely head- and vertex-based schemes on tetrahedra for the NCU_TW-Hybrid_FEM and DTU-FEM_COMSOL, while the highest ones result from the schemes that have head and velocity values as degrees of freedom. Additionally, the ratios of the number of nonzero entries to the number of degrees of freedom exhibit a large variability, ranging from approximately 5 (TPFA on tetrahedrons) to 30 (MPFA schemes with only head degrees of freedom).

5.2. Case 2: Regular fracture network

5.2.1. Description

The second benchmark is a three-dimensional analog of the two-dimensional test case 4.1 from the benchmark study (Flemisch et al., 2018). The domain is given by the unit cube $\Omega = (0\text{m}, 1\text{m})^3$ and contains

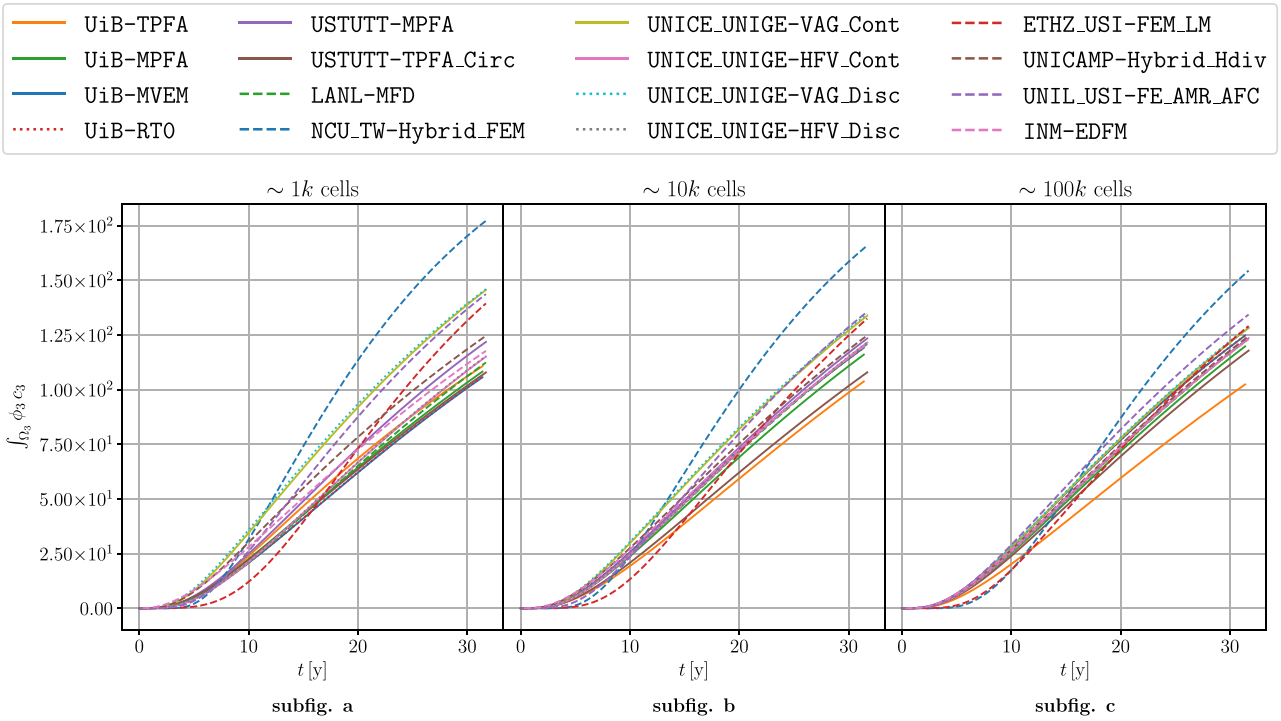

Fig. 5. Case 1 of Section 5.1. Integrated matrix concentration $\int_{\Omega_{3,3}} \phi_3 c_3 \, \mathrm{d}x$ for three refinements (coarse to fine). Results of Section 5.1.2.4.

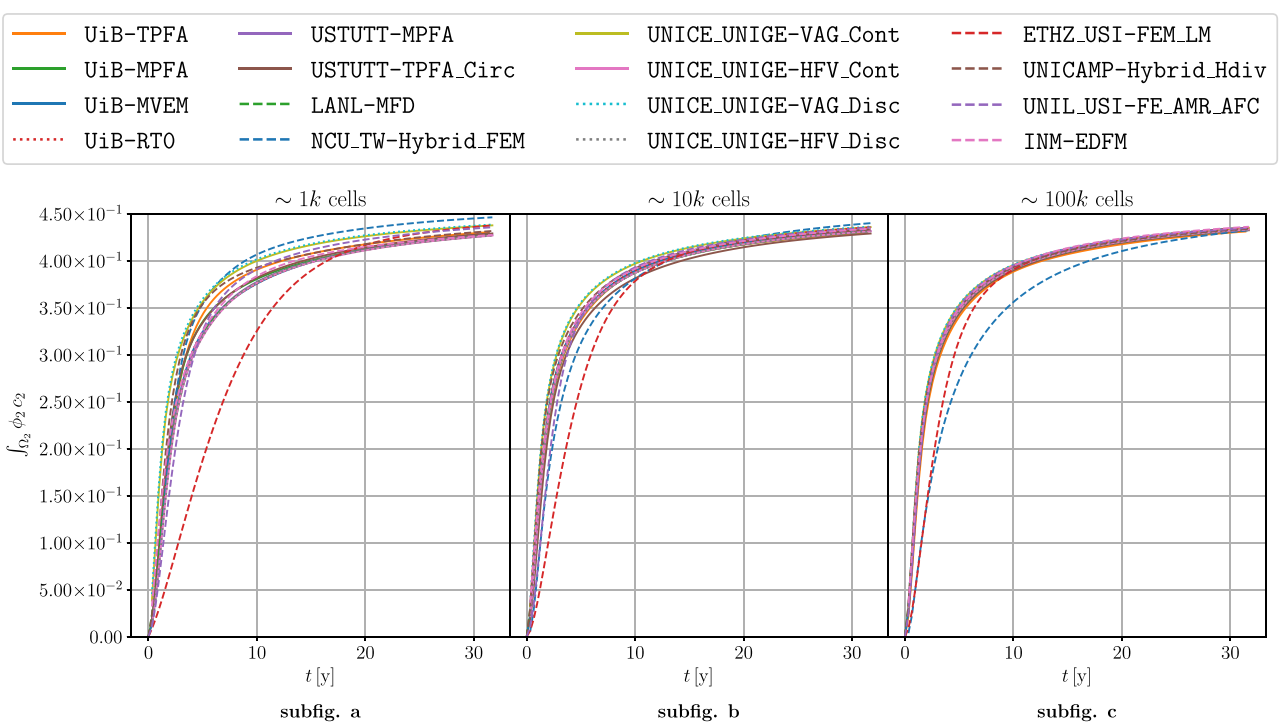

Fig. 6. Case 1 of Section 5.1. Integrated fracture concentration $\int_{\Omega_2} \epsilon_2 \phi_2 c_2 \, \mathrm{d}x$ over time for three refinements (coarse to fine). Results of Section 5.1.2.5.

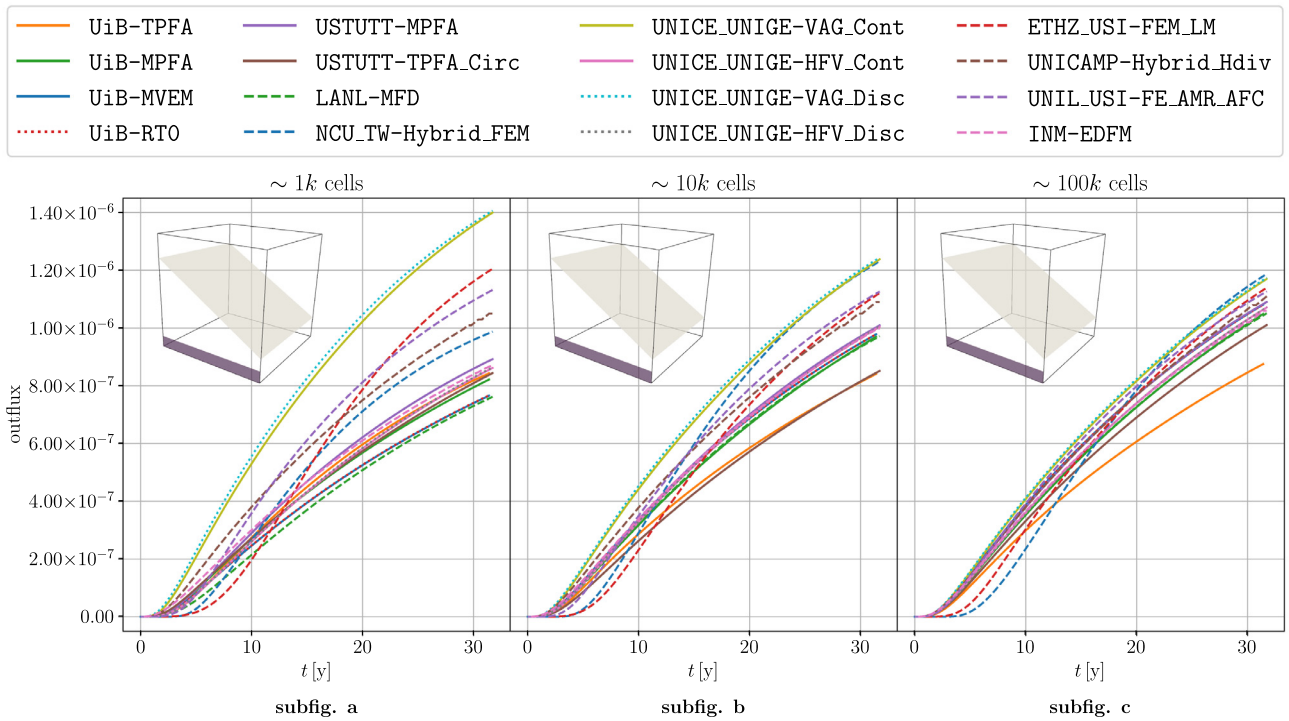

Fig. 7. Case 1 of Section 5.1. Integrated flux of c across the outlet boundary over time for three refinements (coarse to fine). Results of Section 5.1.2.6.

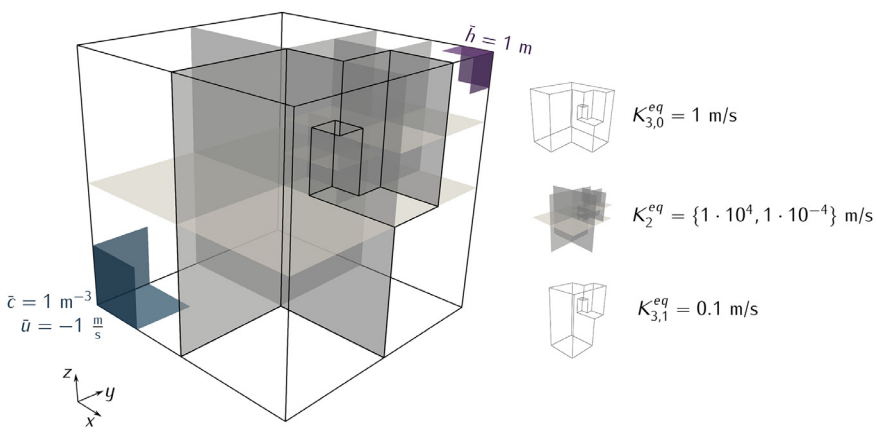

Fig. 8. Representation of the domain ($\Omega_3 = (0\text{m}, 1\text{m})^3$) and the fractures for Case 2 of Section 5.2. The inlet and outlet boundaries are colored in blue and purple, respectively, and on the right side, the permeability distributions among Ω_3 and Ω_2 are illustrated. (For interpretation of the references to color in this figure legend, the reader is referred to the web version of this article.)

9 regularly oriented fractures, as illustrated in Fig. 8. The boundary $\partial\Omega$ is decomposed into three parts, each corresponding to a chosen boundary condition (see Fig. 8). First, $\partial\Omega_h = \{(x, y, z) \in \partial\Omega : x, y, z > 0.875\text{m}\}$ is the part of the boundary where $\bar{h} = 1\text{m}$. Second, a flux boundary condition is set on $\partial\Omega_{in} = \{(x, y, z) \in \partial\Omega : x, y, z < 0.25\text{m}\}$ by imposing $\bar{u} = -1\text{m/s}$. On the remainder of the boundary of Ω, no-flow conditions are imposed.

Two variants of the test case are considered: Case 2.1 has highly conductive fractures and Case 2.2 has blocking fractures. In both cases, different hydraulic conductivities are prescribed in the following matrix subregions:

$$\begin{aligned}
\Omega_{3,0} &= \Omega_3 \setminus \Omega_{3,1} \\
\Omega_{3,1} &= \{(x, y, z) \in \Omega_3 : x > 0.5\text{m} \cap y < 0.5\text{m}\} \\
&\quad \cup \{(x, y, z) \in \Omega_3 : x > 0.75\text{m} \cap 0.5\text{m} < y < 0.75\text{m} \cap z > 0.5\text{m}\} \\
&\quad \cup \{(x, y, z) \in \Omega_3 : 0.625\text{m} < x < 0.75\text{m} \cap 0.5\text{m} \\
&\quad < y < 0.625\text{m} \cap 0.5\text{m} < z < 0.75\text{m}\}.
\end{aligned}$$

The right part of Fig. 8 illustrates these regions. A complete overview of the parameters used in this test case is given in Table 4.

Finally, for the transport problem, a unitary concentration is imposed at the inflow boundary $\partial\Omega_{in}$.

5.2.2. Results

The results were collected for a sequence of 3 simulations by discretizing the 3d domain using approximately 500, 4k, and 32k cells. The number of cells and degrees of freedom used by the participating methods are reported in Table A.8. In the following, results are discussed on the basis of line profiles of the hydraulic head in the 3d matrix as well as plots of the average concentrations within specified subregions of the 3d matrix.

5.2.2.1. Hydraulic Head Over Line. Fig. 9 shows the hydraulic head h_3 plotted along the diagonal line segment (0m, 0m, 0m)-(1m, 1m, 1m) for all grid refinements and for both Case 2.1 and Case 2.2. In the case of conductive fractures the spread and the differences to the reference solution decrease significantly upon grid refinement, although some noticeable differences still prevail for the finest grid.

Table 4
Parameters used in Case 2 of Section 5.2.

	Case 2.1		Case 2.2	
Matrix hydraulic conductivity $K_3\|_{\Omega_{3,0}}$	$\boldsymbol{I}$	m/s	$\boldsymbol{I}$	m/s
Matrix hydraulic conductivity $K_3\|_{\Omega_{3,1}}$	$1\times10^{-1}\boldsymbol{I}$	m/s	$1\times10^{-1}\boldsymbol{I}$	m/s
Fracture effective tangential hydraulic conductivity K_2	$\boldsymbol{I}$	m²/s	$1\times10^{-8}\boldsymbol{I}$	m²/s
Fracture effective normal hydraulic conductivity κ_2	2×10^{8}	1/s	2	1/s
Intersection effective tangential hydraulic conductivity K_1	1×10^{-4}	m³/s	1×10^{-12}	m³/s
Intersection effective normal hydraulic conductivity κ_1	2×10^{4}	m/s	2×10^{-4}	m/s
Intersection effective normal hydraulic conductivity κ_0	2	m²/s	2×10^{-8}	m²/s
Matrix porosity ϕ_3	1×10^{-1}		1×10^{-1}	
Fracture porosity ϕ_2	9×10^{-1}		1×10^{-2}	
Intersection porosity ϕ_1	9×10^{-1}		1×10^{-2}	
Fracture cross-sectional length ϵ_2	1×10^{-4}	m	1×10^{-4}	m
Intersection cross-sectional area ϵ_1	1×10^{-8}	m²	1×10^{-8}	m²
Intersection cross-sectional volume ϵ_0	1×10^{-12}	m³	1×10^{-12}	m³
Total simulation time	2.5×10^{-1}	s		
Time-step Δt	2.5×10^{-3}	s		

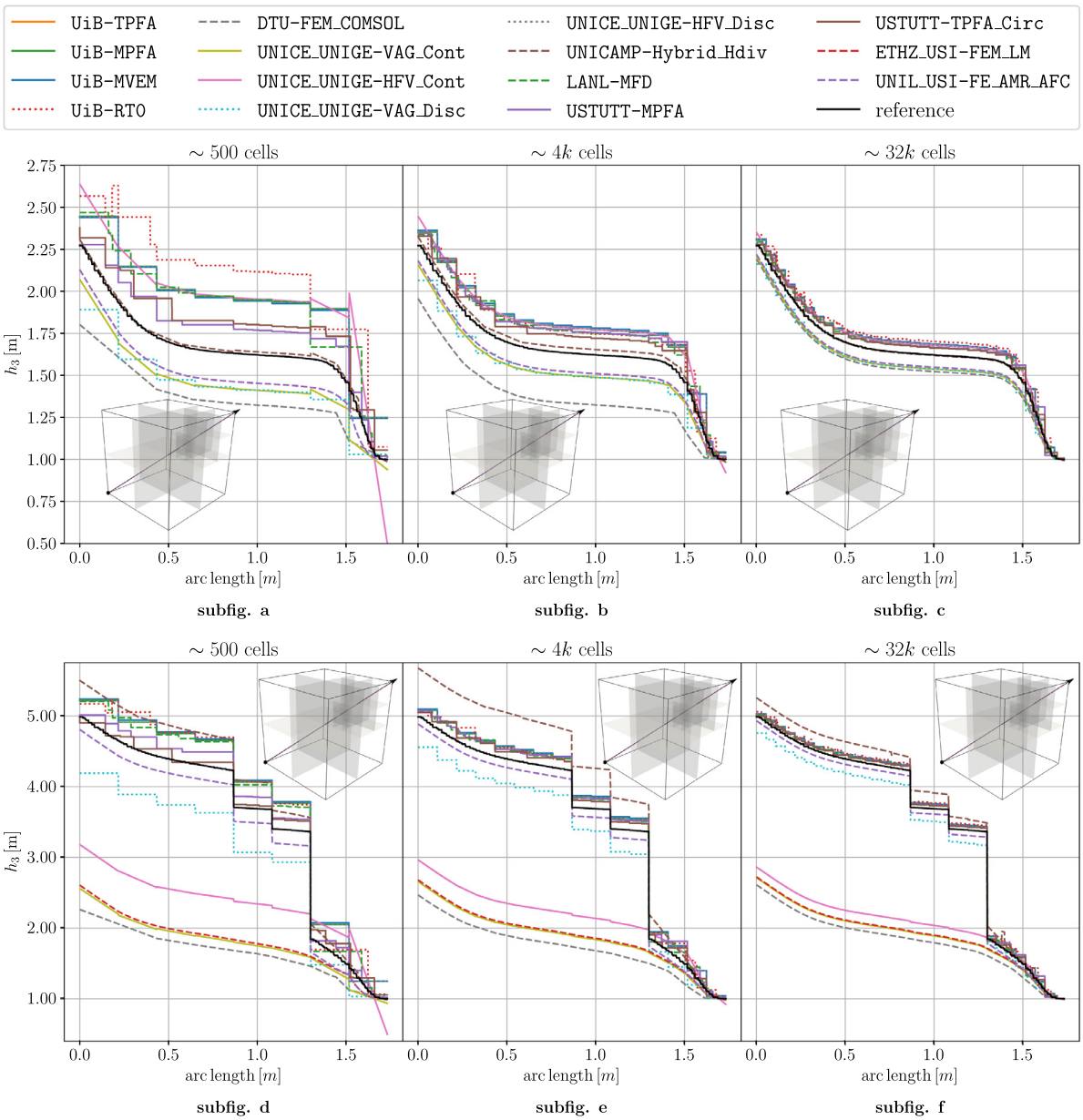

Fig. 9. Case 2 of Section 5.2. Plots of the hydraulic head h_3 along the line (0m, 0m, 0m) - (1m, 1m, 1m) for the different refinement levels (grid refinement increases from left to right) for the case of conductive fractures (Case 2.1, upper row) and blocking fractures (Case 2.2, lower row). The reference was computed with the USTUTT-MPFA scheme on a refined grid with 1,046,566 cells. Results of Section 5.2.2.1.

In the case of blocking fractures, the highest discrepancies are shown by the schemes that assume continuity of the hydraulic head across the fractures. As expected, these methods cannot capture the jump in the hydraulic head present in this test case. On the other hand, the remaining schemes approach the reference solution. The UNICE_UNIGE-VAG_Disc and the UNIL_USI-FE_AMR_AFC produce slightly lower and the UNICAMP-Hybrid_Hdiv scheme slightly higher hydraulic heads, but the deviations tend to diminish with increasing grid refinement.

The UNICE_UNIGE-VAG_Cont and UNICE_UNIGE-VAG_Disc methods incorporate Dirichlet boundary conditions on the vertices rather than on faces. This may explain, in part, the deviations in hydraulic head observed on coarse meshes for these methods. As expected, these differences decrease with mesh refinement. For the UNIL_USI-FE_AMR_AFC method, the differences might come from the representation of the fractures, which have the same spatial dimension as the background matrix. In particular, each fracture consists of a layer of elements that is refined at least twice by using adaptive mesh refinement.

5.2.2.2. Mean Matrix Concentration Over Time. The second comparison in Case 2 concerns the solution of the transport equation over time. These solutions are computed only on the second level of mesh refinement, i.e., using approximately 4000 cells. For the simulation of the transport model, the upwind scheme is employed for all methods except UNIL_USI-FE_AMR_AFC and ETHZ_USI-FEM_LM, which employ a finite element discretization with an algebraic flux correction Kuzmin et al. (2012).

The top of Fig. 10 depicts the temporal evolution of the mean tracer concentrations in three matrix regions for the case of highly conductive fractures. These regions were selected to form a representative illustration of the spread between the schemes. It can be seen that the majority of the schemes produce rather low concentrations in the first region, on the order of 2.5% at the final simulation time. In contrast, the ETHZ_USI-FEM_LM and the UNIL_USI-FE_AMR_AFC schemes produce significantly higher concentrations with values above 10% at the end of the simulation. In general, the temporal evolution of the concentrations in these three regions agrees very well among the majority of participating schemes, while the ETHZ_USI-FEM_LM and the UNIL_USI-FE_AMR_AFC schemes show significant deviations. These might be related to the flow discretization methods, but could also be affected by the different discretization that is employed for the transport discretization related to these methods, and, for UNIL_USI-FE_AMR_AFC, also the underlying equi-dimensional model.

For the case of blocking fractures, the concentrations in the same matrix regions are illustrated in the bottom row of Fig. 10. In general, a larger spread of the computed concentrations can be observed. For the first region, the schemes that assume continuity of the hydraulic head produce significantly lower concentrations, while the remaining schemes produce solutions that agree rather well. However, for the second and third regions, the concentrations at the final simulation time show a wide spread among all participating schemes.

As a general trend, it can be observed that the differences in computed concentrations increase with time. Additionally, differences increase with the regions' distance from the inflow boundary. As expected, for the case of conductive fractures, the differences are smaller than in the case of blocking fractures.

5.3. Case 3: Network with small features

5.3.1. Description

This test case is designed to probe accuracy in the presence of small geometric features, which may cause trouble for conforming meshing strategies. The domain is the box $\Omega = (0\text{m}, 1\text{m}) \times (0\text{m}, 2.25\text{m}) \times (0\text{m}, 1\text{m})$, containing eight fractures (see Fig. 11).

Table 5
Parameters used in Case 3 of Section 5.3.

Matrix hydraulic conductivity K_3	$\boldsymbol{I}$	m/s
Fracture effective tangential hydraulic conductivity K_2	$1 \times 10^2 \boldsymbol{I}$	m^3/s
Fracture effective normal hydraulic conductivity κ_2	2×10^6	1/s
Intersection effective tangential hydraulic conductivity K_1	1	m^2/s
Intersection effective normal hydraulic conductivity κ_1	2×10^4	m/s
Matrix porosity ϕ_3	2×10^{-1}	
Fracture porosity ϕ_2	2×10^{-1}	
Intersection effective porosity ϕ_1	2×10^{-1}	
Fracture cross-sectional length ϵ_2	1×10^{-2}	m
Intersection cross-sectional area ϵ_1	1×10^{-4}	m^2
Total simulation time	1×10^0	s
Time-step Δt	1×10^{-2}	s

The inlet and outlet boundaries are defined as follows:

$$\begin{aligned}
\partial\Omega_N &= \partial\Omega \setminus \left(\partial\Omega_{in} \cup \partial\Omega_{out}\right) \\
\partial\Omega_{in} &= (0\text{m}, 1\text{m}) \times \{0\text{m}\} \times (1/3\text{m}, 2/3\text{m}) \\
\partial\Omega_{out} &= \partial\Omega_{out,0} \cup \partial\Omega_{out,1} \\
\partial\Omega_{out,0} &= (0\text{m}, 1\text{m}) \times \{2.25\text{m}\} \times (0\text{m}, 1/3\text{m}) \\
\partial\Omega_{out,1} &= (0\text{m}, 1\text{m}) \times \{2.25\text{m}\} \times (2/3\text{m}, 1\text{m})
\end{aligned}$$

The boundary conditions for flow are zero Dirichlet conditions on $\partial\Omega_{out}$ and uniform unit inflow on $\partial\Omega_{in}$, so that $\int_{\partial\Omega_{in}} \mathbf{u}_3 \cdot \mathbf{n} dS = -1/3\text{m}^2/\text{s}$, and zero Neumann conditions on $\partial\Omega_N$. For the transport problem, the initial condition is zero in Ω, and the boundary condition is a unit concentration at $\partial\Omega_{in}$. A complete overview of the parameters used in Case 3 is given in Table 5.

5.3.2. Results

Similar to the previous cases, the methods are compared on the basis of a) the hydraulic head of the matrix domain along two lines, b) the integrated fracture concentration over time, c) the fluxes out of the domain and d) computational cost. Two different simulations with approximately 30k and 150k cells for the 3d domain were performed. It was seen as infeasible to include one more level of refinement for all methods. However, refined versions of the USTUTT-MPFA with up to approximately 10^6 matrix cells were produced. At this stage, there were no noticeable differences between solutions on different grids, and the finest solution was included as a reference solution.

5.3.2.1. Hydraulic Head Over Line. Fig. 12 shows the profile of the hydraulic head h_3 in the matrix along the line $(0.5\text{m}, 1.1\text{m}, 0\text{m}) - (0.5\text{m}, 1.1\text{m}, 1\text{m})$. This shows considerable differences between the methods for both refinement levels. However, the agreement is better for the second refinement level, where most of the methods are within a relative hydraulic head range of approximately 10%. The UNICE_UNIGE-VAG_Disc, UNICE_UNIGE-VAG_Cont, DTU-FEM_COMSOL, and UNIL_USI-FE_AMR_AFC methods show the highest discrepancies in these plots, but the deviation from the reference solution decreases significantly with higher refinement. The significant difference between the refinements may indicate that the small features of the fracture network geometry are not adequately resolved, at least not by the coarser grids. This is in line with the purpose of the test case.

5.3.2.2. Mean Fracture Concentration Over Time. Data were reported for the integrated concentration $\overline{c_2} = \int_{\Omega_{2,i}} c_2 / |\Omega_{2,i}|$ on each fracture i throughout the simulation. There is a general agreement between the methods, with the method of ETHZ_USI-FEM_LM showing some deviations for some of the fractures. As an example, Fig. 13 shows the plots for both refinement levels for fracture number 3, demonstrating limited difference between the refinement levels.

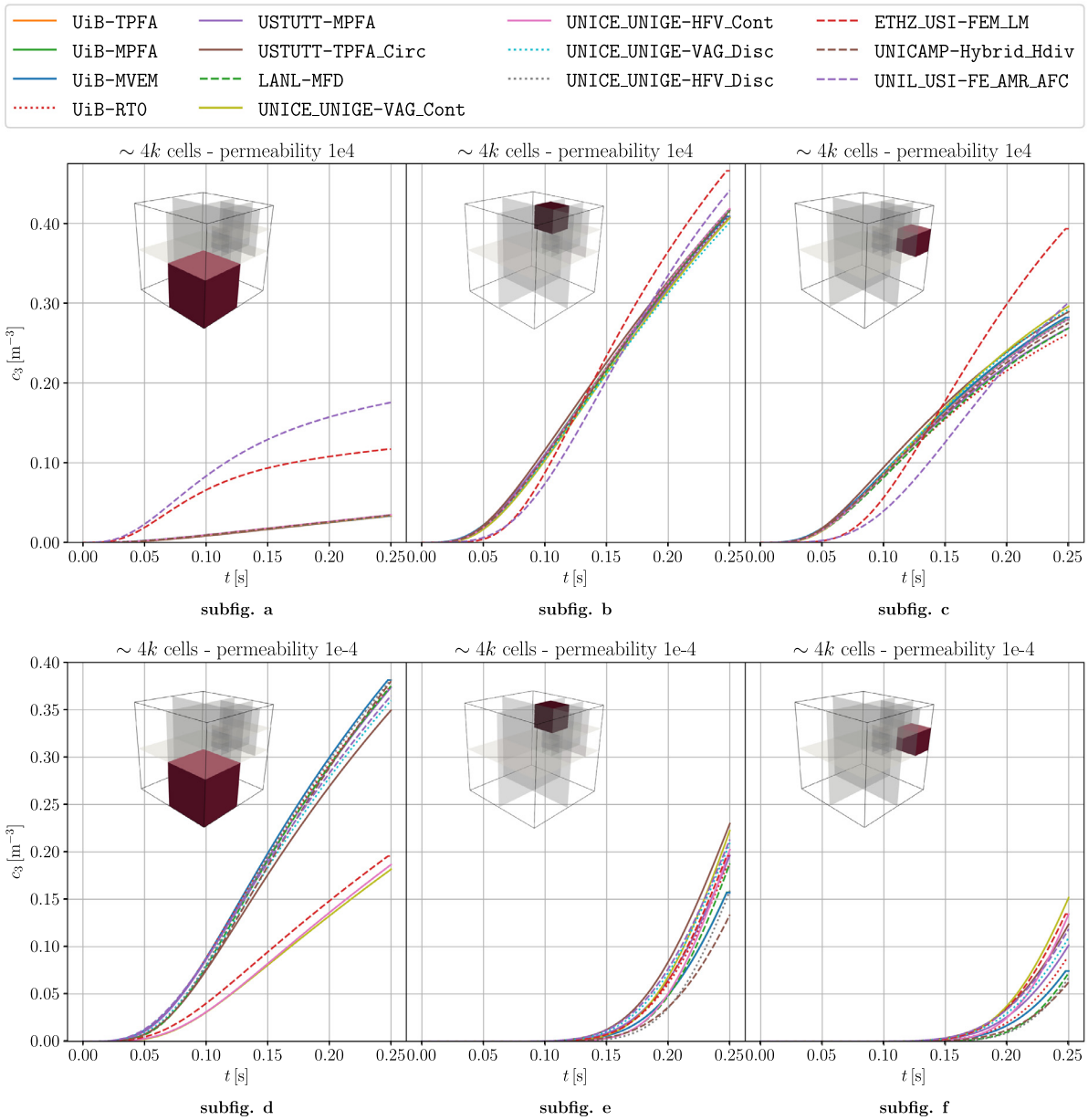

Fig. 10. Case 2 of Section 5.2. On the top, temporal evolution of the average tracer concentration in matrix regions 1, 10 and 11 (from left to right) for the case of conductive fractures (Case 2.1). On the bottom, temporal evolution of the average tracer concentration in the matrix regions 1, 10 and 11 (from left to right) for the case of blocking fractures (Case 2.2). Results of Section 5.2.2.2.

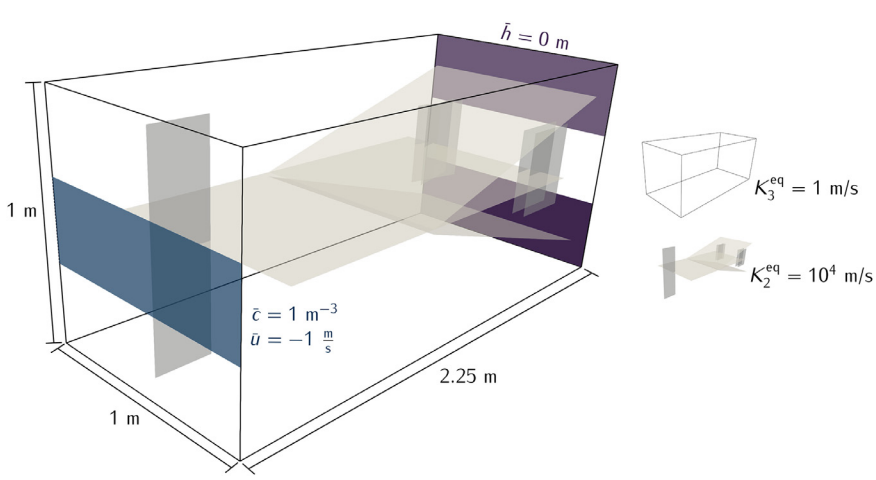

Fig. 11. Representation of the fractures and the outline of the domain for Case 3 of Section 5.3.

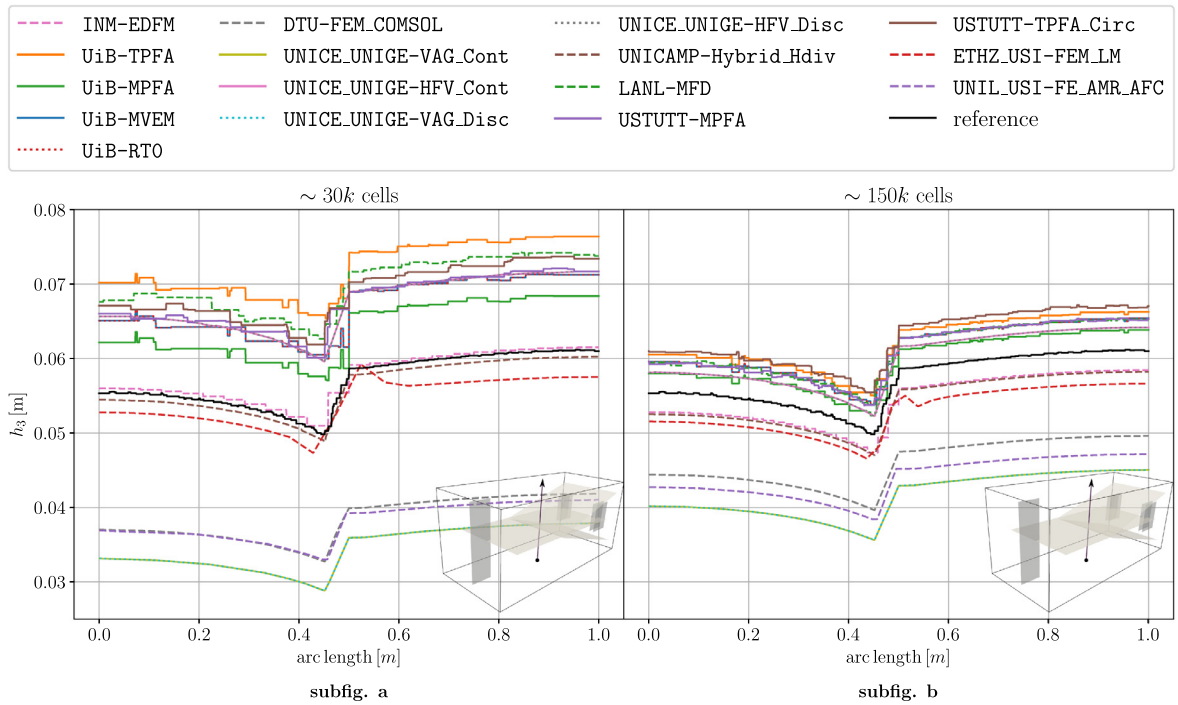

Fig. 12. Case 3 of Section 5.3. Hydraulic head h_3 in the matrix over the line $(0.5\text{m}, 1.1\text{m}, 0\text{m}) - (0.5\text{m}, 1.1\text{m}, 1\text{m})$ for the coarse (left) and fine (right) grid. The solid black line shows the solution obtained with the USTUTT-MPFA scheme on a grid with approximately 10^6 matrix cells. Results of Section 5.3.2.1.

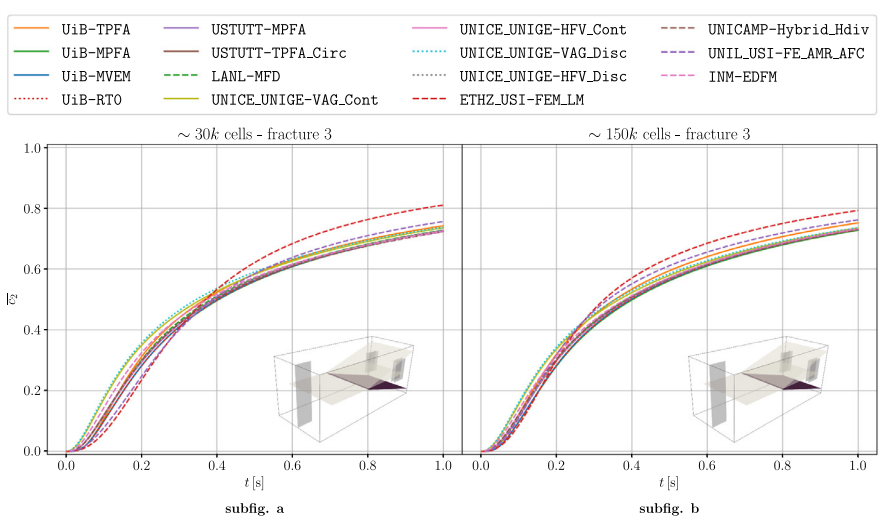

Fig. 13. Case 3 of Section 5.3. Mean concentration within fracture number 3 throughout the simulation time for the coarse (left) and fine (right) grid. Results of Section 5.3.2.2.

5.3.2.3. Boundary Fluxes. The total outflow $\overline{u}_{out} = \int_{\partial\Omega_{out}} \boldsymbol{u}_3 \cdot \boldsymbol{n} dS$ and the proportion exiting over $\partial\Omega_{out,0}$, i.e., $r_{out} = \int_{\partial\Omega_{out,0}} \boldsymbol{u}_3 \cdot \boldsymbol{n} dS / \overline{u}_{out}$, are shown in Fig. 14. When compared to the prescribed inflow of -1/3m^3/s, the $\overline{u}_{out}$ values reveal a small lack of volume conservation for ETHZ_USI-FEM_LM, but the method improves for the finer grid. The ratio r_{out} provides an indication of whether the flux fields agree. The ratios generally agree well with the refined USTUTT-MPFA, except for the ETHZ_USI-FEM_LM method, which does not approach the reference value for the finest grid.

5.3.2.4. Computational Cost. Based on the data presented in Table A.9, note that the UNIL_USI-FE_AMR_AFC applies 68k and 203k cells for the cases where 30k and 150k cells were prescribed, respectively. The rest of the methods are well within 10% of the prescribed values. As for the other test cases, there are significant variations in the number of degrees of freedom and nonzero matrix entries related to the design of the methods.

5.4. Case 4: Field case

5.4.1. Description

The geometry of the fourth case is based on a postprocessed outcrop from the island of Algerøyna, outside Bergen, Norway, and is a subset of the fracture network presented in Fumagalli et al. (2019). From the outcrop, 52 fractures were selected, extruded in the vertical direction and then cut by a bounding box. The resulting network has 106 fracture intersections, and multiple fractures intersect the domain boundary.

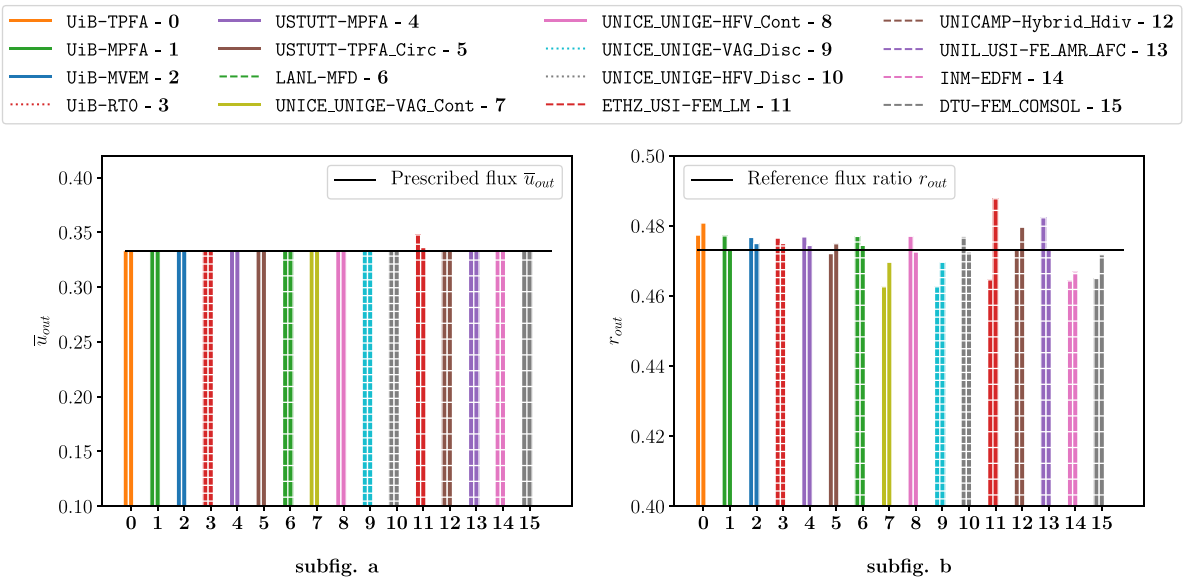

Fig. 14. Case 3 of Section 5.3. Total outflux (left) and ratio exiting over $\partial\Omega_{out,0}$ (right). The bar pairs correspond to the coarse and fine grid, while the reference solution is indicated by the horizontal line. Results of Section 5.3.2.3.

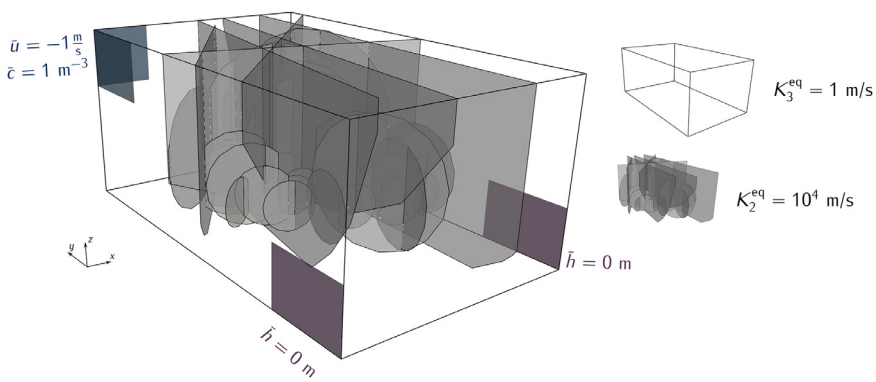

Fig. 15. Case 4 of Section 5.4. Representation of the fractures and the outline of the domain. Inlet boundaries are shown in blue, outlets in purple. (For interpretation of the references to color in this figure legend, the reader is referred to the web version of this article.)

The simulation domain is the box $\Omega = (-500\text{m}, 350\text{m}) \times (100\text{m}, 1500\text{m}) \times (-100\text{m}, 500\text{m})$. The fracture geometry is depicted in Fig. 15.

The inlet and outlet boundaries are defined as follows:

$$\begin{aligned}
\partial\Omega_N &= \partial\Omega \setminus \left(\partial\Omega_{in} \cup \partial\Omega_{out}\right),\\
\partial\Omega_{in} &= \partial\Omega_{in,0} \cup \partial\Omega_{in,1}, \qquad \partial\Omega_{out} = \partial\Omega_{out,0} \cup \partial\Omega_{out,1},\\
\partial\Omega_{in,0} &= (-500\text{m}, -200\text{m}) \times \{1500\text{m}\} \times (300\text{m}, 500\text{m}),\\
\partial\Omega_{in,1} &= \{-500\text{m}\} \times (1200\text{m}, 1500\text{m}) \times (300\text{m}, 500\text{m}),\\
\partial\Omega_{out,0} &= \{-500\text{m}\} \times (100\text{m}, 400\text{m}) \times (-100\text{m}, 100\text{m}),\\
\partial\Omega_{out,1} &= \{350\text{m}\} \times (100\text{m}, 400\text{m}) \times (-100\text{m}, 100\text{m}).
\end{aligned}$$

The boundary conditions for flow are zero Dirichlet conditions on $\partial\Omega_{out}$ and uniform unit inflow on $\partial\Omega_{in}$, so that $\int_{\partial\Omega_{in}} \mathbf{u}_3 \cdot \mathbf{n} dS = -1.2e5\text{m}^3/\text{s}$, and zero Neumann conditions on $\partial\Omega_N$. For the transport problem, the initial condition is zero in Ω, and the boundary condition is a unit concentration at $\partial\Omega_{in}$. The parameters for conductivity, porosity and aperture are given in Table 6, as is the total simulation time and time-step size.

Because of the complex network geometry, grid refinement studies were considered infeasible and the benchmark specified the usage of a single grid. A Gmsh (Geuzaine and Remacle, 2009) configuration file was provided to assist participants with geometry processing and meshing. The use of this predefined grid was optional, but the number of 3d cells should be approximately 260k.

Table 6
Parameter used in Case 4 of Section 5.4.

Matrix hydraulic conductivity K_3	$\boldsymbol{I}$	m/s
Fracture effective tangential hydraulic conductivity K_2	$1 \times 10^2 \boldsymbol{I}$	m^3/s
Fracture effective normal hydraulic conductivity κ_2	2×10^6	1/s
Intersection effective tangential hydraulic conductivity K_1	1	m^2/s
Intersection effective normal hydraulic conductivity κ_1	2×10^4	m/s
Matrix porosity ϕ_3	2×10^{-1}	
Fracture porosity ϕ_2	2×10^{-1}	
Intersection porosity ϕ_1	2×10^{-1}	
Fracture cross-sectional length ϵ_2	1×10^{-2}	m
Intersection cross-sectional area ϵ_1	1×10^{-4}	m^2
Total simulation time	5×10^3	s
Time-step Δt	5×10^1	s

5.4.2. Results

Results were reported for 14 schemes. The two methods that participated in Case 3, which is closest in geometric complexity, but not in Case 4, are `INM-EDFM` and `UNIL_USI-FE_AMR_AFC`. The participating methods are compared in terms of a) hydraulic head of the matrix domain along two lines, b) time series of concentrations in selected fractures and c) computational cost.

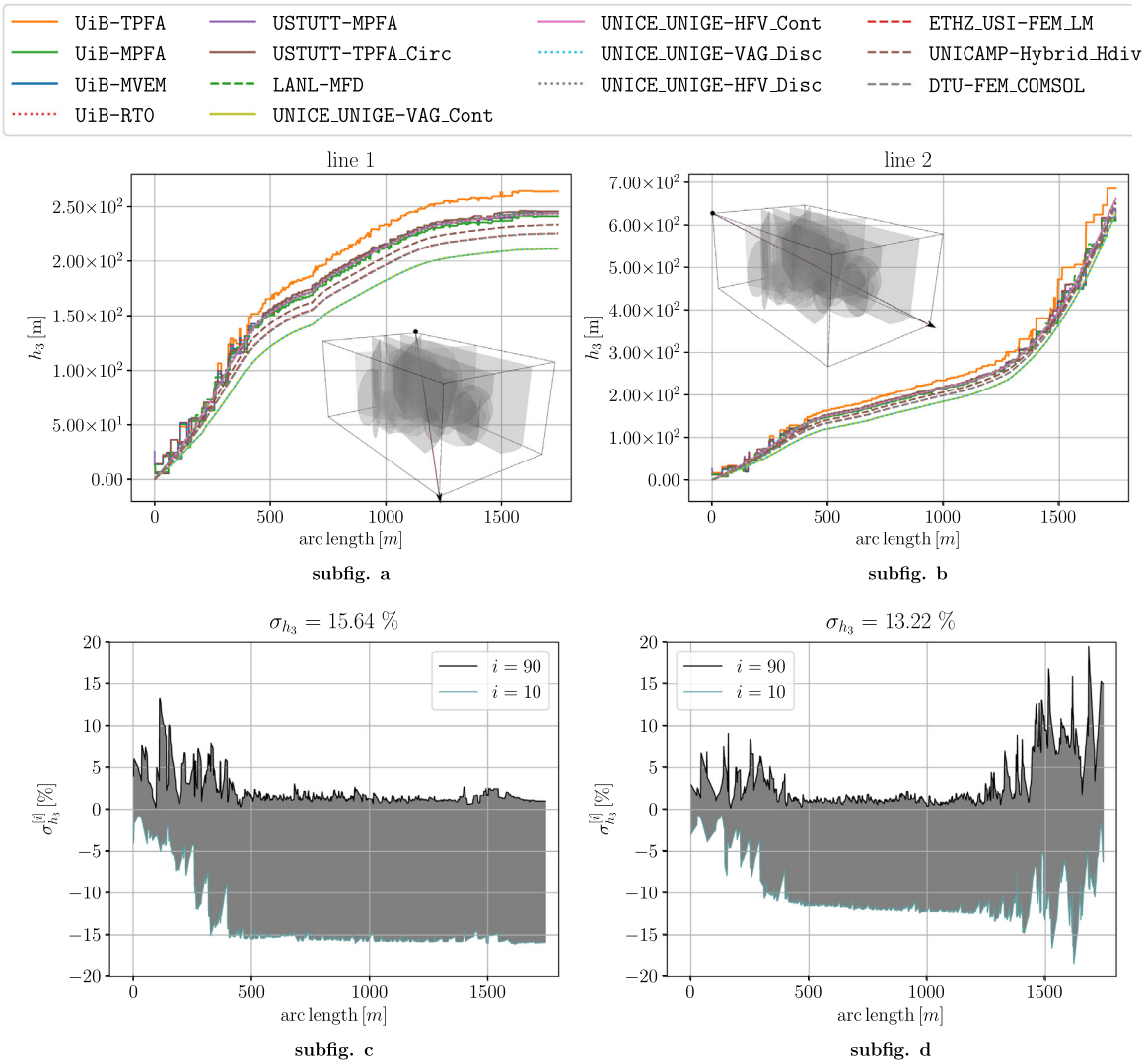

Fig. 16. Case 4 of Section 5.4. Hydraulic head profiles across the domain. Left: Profile from outlet $\partial\Omega_{out,0}$ towards the opposite corner. Right: Profile from outlet $\partial\Omega_{out,1}$ towards $\partial\Omega_{in}$. On the bottom, the deviations $\sigma_{h_3}^{[90]}$ and $\sigma_{h_3}^{[10]}$ are illustrated, as defined in (16). Here, the median $h_3^{[50]}$ of the solutions on the finest grid is used as the reference solution h_3^{ref}. Results of Section 5.4.2.1.

5.4.2.1. Hydraulic Head. Fig. 16 shows the hydraulic head along the two specified lines, together with the spread of the reported results. Both lines start in points at the outflow boundaries where the hydraulic head is set to 0; the first line ends far away from the inlet, while the second ends at the inlet boundary. For the first line there are noticeable deviations for some of the solutions: The `UiB-TPFA` scheme predicts a significantly higher hydraulic head drop, likely caused by the inconsistency of the scheme. Conversely, the `UNICE_UNIGE-VAG_Disc` and `UNICE_UNIGE-VAG_Cont` methods underestimate the drop in hydraulic head compared to the average of the reported results, while there is only minor disagreement among the other methods. On the second line, the `UiB-TPFA` scheme overestimates the drop in hydraulic head over the domain, while the other methods are in very good agreement. The average spread σ_{h_3} calculated according to (16) of around 15% is within a reasonable range, considering the geometrical complexity of the fracture network.

5.4.2.2. Concentration Plots. The quality of the flux field is measured by the time series of average concentrations in the fracture planes, with good agreement among most of the methods. Fig. 17 shows the time evolution of concentration for three of the fractures, numbers 15, 45 and 48, which show the largest differences between the methods. The results produced by the `ETHZ_USI-FEM_LM` deviate slightly from the other methods on two of these figures, while `UNICE_UNIGE-VAG_Disc` also shows a slight deviation for one of the figures.

5.4.2.3. Computational Cost. Measures for the computational cost of the participating methods are given in Table A.10. Most of the groups used the provided mesh file. The `UNICAMP-Hybrid_Hdiv` method used a grid with only approximately 40% of the cells in the provided grid. `DTU-FEM_COMSOL` employed almost seven times more 3d cells for its nodal-based method, yielding a number of degrees of freedom that is in the lower half with respect to all participating methods. As in the previous test cases, there are significant differences in the number of unknowns and nonzero matrix elements among the methods.

6. Summary of results

The performance of each method for all test cases is indicated in Fig. 18. The main points emerging from the discussion of the results in Section 5 are:

1. Of the 17 schemes that participated in at least one of the test cases, 14 presented simulation results on all four cases.

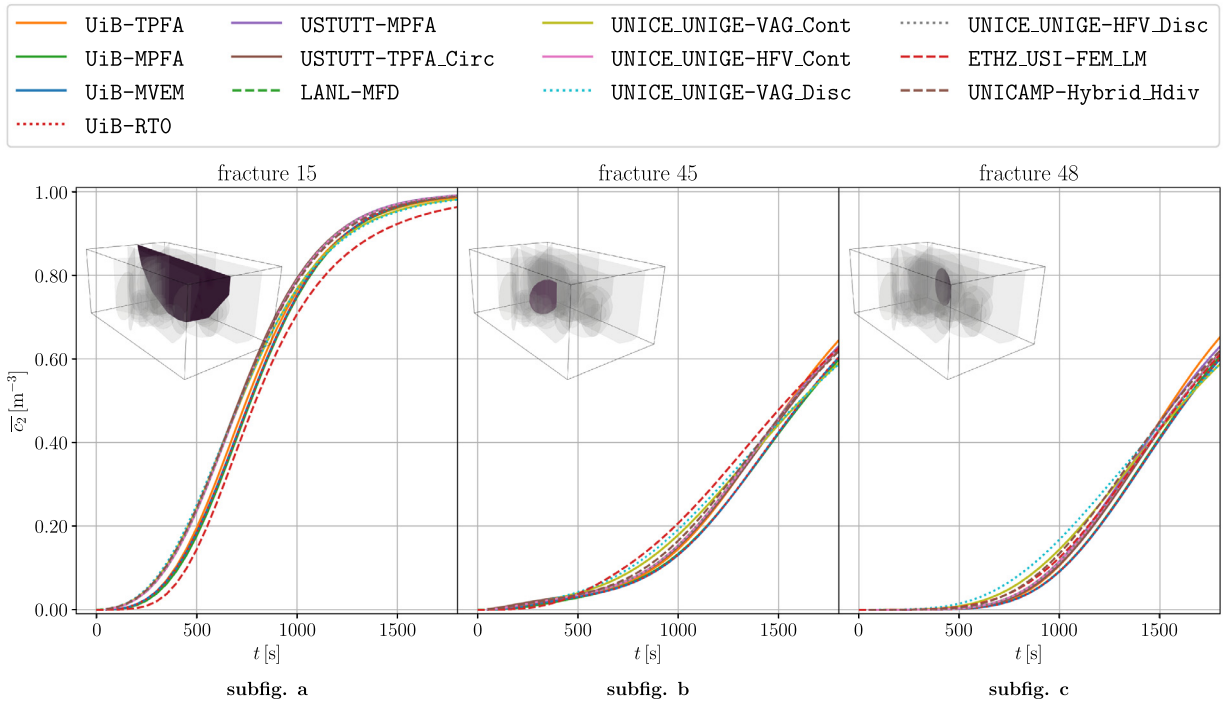

Fig. 17. Case 4 of Section 5.4. Mean concentration over time in three selected fractures with identification 15, 45, and 48. Results of Section 5.4.2.2.

No significant deviation
Minor deviation
Major deviation
No results reported

Method	Case 1						Case 2				Case 3				Case 4		
	a	b	c	d	e	f	a1	a2	b1	b2	a	b	c	d	a	b	c
UiB-TPFA																	
UiB-MPFA																	
UiB-MVEM																	
UiB-RT0																	
USTUTT-MPFA																	
USTUTT-TPFA_Circ																	
LANL-MFD																	
NCU_TW-Hybrid_FEM																	
UNICE_UNIGE-VAG_Cont																	
UNICE_UNIGE-HFV_Cont																	
UNICE_UNIGE-VAG_Disc																	
UNICE_UNIGE-HFV_Disc																	
ETHZ_USI-FEM_LM																	
UNICAMP-Hybrid_Hdiv																	
UNIL_USI-FE_AMR_AFC																	
INM-EDFM																	
DTU-FEM_COMSOL																	

Fig. 18. Summary of the performance of all methods.

2. Cases 3 and 4 pose the highest demands on the methods in terms of geometrical complexity. Taken together, the cases point to the challenges inherent to DFM simulations and indicate the methods' robustness in this respect.
3. Although the prescribed numbers of cells was adhered to for most of the methods, the numbers of degrees of freedom and matrix density reported in Tables A.7 through A.10 vary significantly, indicating differences in computational cost.
4. Not unexpectedly, fractures that act as barriers cause trouble for the methods that assume a continuous hydraulic head over the fracture, as seen in Case 2. Blocking fractures are outside the intended range of validity for these models, and alternative approaches should be sought for those cases.
5. Out of the 17 schemes, one is not mass conservative. There are no signs of the lack of conservation in the reported concentration fields, likely due to successful postprocessing of the flux fields. Nevertheless, for most of the test cases, the concentration fields reported by the nonconforming mesh method `ETHZ_USI-FEM_LM` deviate from the other reported results.
6. The well-known inconsistency of the widely used two-point flux approximation is manifested in the underestimation of permeability in the hydraulic head results reported for `UiB-TPFA`. The

`USTUTT-TPFA_Circ` method circumvents this inconsistency by locating the hydraulic head values at the circumcenters of the tetrahedrons. However, this poses additional restrictions on the mesh.

The observations herein can to some degree be used as guidance when choosing discretization schemes for practical simulations, with the 7 methods that showed no deviations on any of the benchmark methods being natural candidates. Nevertheless, said observations should not be uncritically transferred to other geometries, problem setups and quantities of interest. The choice of discretization method can also be influenced by aspects not discussed in this benchmark, such as the availability of efficient linear solvers and the ease of implementation. Moreover, the participating methods obviously don't cover the whole range of available DFM discretization approaches.

7. Conclusion and outlook

This paper has presented a set of benchmark cases for the simulation of flow in three-dimensional fractured porous media, assuming Darcy flow in both matrix and fractures. The suite consists of one case with a single fracture, one case with 9 fractures and setups with conductive and blocking fractures, one case with 8 fractures designed to emphasize complex geometric details, and finally a case with 52 fractures, based on a real fracture network. The metrics employed to measure discretization performance are a) the profiles of the hydraulic head, b) the quality of the flux field measured by simulation of passive tracers and c) the computational cost as indicated by the number of degrees of freedom and matrix sparsity pattern. A total of 17 methods participated in the benchmark. While these can't include all discretization schemes proposed for flow in fractured porous media, they nevertheless cover a wide range of numerical approaches.

The benchmark uncovered important differences between the methods, with 10 methods showing significant deviations. While the observations and discussions herein offer some guidance to identifying well-suited methods for practical simulations, such extrapolation requires care and consideration of the particularities of the simulation in question. Moreover, the high number of participating methods and research groups proves that simulations in 3d media are fully feasible for a wide range of schemes and research codes. For further development of discretization methods, 3d cases should therefore become a natural complement to the more traditional 2d simulation results.

To advance the field of numerical methods for physics-based models, there is a need both for creative development of new mathematical models and numerical methods and for rigorous testing and comparison. The current paper presents a contribution to the latter. The provided test cases and data provides researchers with a suite of problems to benchmark methods and implementations for single-phase flow in fractured porous media. With this, researchers in the field are invited to utilize the test cases, results and data from the current study in development of new methods. Further, with recent developments of models and numerical methods for more complex and coupled physics in fractured porous media, the present work can hopefully also serve as inspiration for development of additional benchmark studies in the future.

CRediT author statement

I. Berre, W. Boon, B. Flemisch, A. Fumagalli, D. Gläser, E. Keilegavlen, A. Scotti, I. Stefansson, and A. Tatomir were jointly responsible for conceptualizing, initiating and coordinating the whole benchmark process as described in Section 2. They wrote the initial draft of the manuscript and were responsible for the overall review and editing process. In the roles outlined in Section 2, the following authors acted as "designers" and "coordinators" for the individual benchmark cases:

Case	Designer(s)	Coordinator(s)
1	D. Gläser, A. Tatomir	B. Flemisch, A. Tatomir
2	A. Fumagalli, I. Stefansson	W. Boon, D. Gläser
3	E. Keilegavlen, I. Stefansson	I. Stefansson, A. Fumagalli
4	E. Keilegavlen, A. Fumagalli	E. Keilegavlen

All other authors mainly acted as benchmark participants for one or more discretization methods. This included implementing and executing the benchmark case scenarios, post-processing and uploading the results as well as communicating with the coordinating group. Acting as internal reviewers, they were also involved in editing the manuscript. The following table lists the persons responsible for the participating methods, which naturally also includes authors from the coordinating group:

Author(s)	Method(s)
K. Brenner, J. Hennicker, R. Masson	`UNICE_UNIGE-*`
S. Burbulla	`USTUTT-TPFA_Circ`
P. Devloo, O. Duran	`UNICAMP-Hybrid_Hdiv`
M. Favino, M. Nestola	`UNIL_USI-FE_AMR_AFC`
A. Fumagalli, E. Keilegavlen, I. Stefansson	`UiB-*`
D. Gläser	`USTUTT-MPFA`
I.-H. Lee, C.-F. Ni	`NCU_TW-Hybrid_FEM`
K. Lipnikov, D. Svyatskiy	`LANL-MFD`
K. Mosthaf	`DTU-FEM_COMSOL`
K. Nikitin, R. Yanbarisov	`INM-EDFM`
P. Schädle, P. Zulian	`ETHZ_USI-FEM_LM`

Declaration of Competing Interest

The authors declare that they have no known competing financial interests or personal relationships that could have appeared to influence the work reported in this paper.

Acknowledgments

I. Berre, A. Fumagalli, E. Keilegavlen, and I. Stefansson were supported by Norwegian Research Council grants 250223, 244129/E20 and 267908/E20. The contribution of *S. Burbulla* was funded by the Deutsche Forschungsgemeinschaft (DFG, German Research Foundation) - Project Number 327154368 - SFB 1313. *P. Devloo* was supported by Fapesp grant No 2017/15736-3, ANP/Petrobras grant No 2014/00090-2 and CNPq grant No 310369/2006-1. *O. Duran* was supported by ANP/Petrobras grant No 2014/00090-2. *M. Favino* was supported by the Swiss National Science Foundation (SNSF) grant PZ00P2_180112. *M. Nestola and P.Zulian* were supported by the SCCER-SoE and the Pasc Project FASTER. *C.-F. Ni and I.-H. Lee* were partially funded by Institute of Nuclear Energy Research under grant NL1050288 and by Ministry of Science and Technology under grant MOST 108-2116-M-008-004- and MOST 106-2116-M-008-014-. *K. Nikitin and R. Yanbarisov* were supported by Moscow Center for Fundamental and Applied Mathematics (agreement with the Ministry of Education and Science of the Russian Federation No. 075-15-2019-1624). *P. Schädle* thanks the Werner Siemens Foundation for their endowment of the Geothermal Energy and Geofluids group at the Institute of Geophysics, ETH Zurich.

Appendix A. Measures of Computational Cost

This section provides three indicators related to computational cost: the number of cells (0d-3d), the number of degrees of freedom and the number of nonzero matrix entries. There is one table for each test case with data of all the participating methods at all refinement levels. For the equi-dimensional `UNIL_USI-FE_AMR_AFC` method, the cells

Table A.7
Computational cost indicators for Case 1.

Method	Refinement	0d cells	1d cells	2d cells	3d cells	dofs	nnz
	0	0	0	112	1,022	1,358	6,008
UiB-TPFA	1	0	0	756	9,438	11,706	53,904
	2	0	0	4,576	98,311	112,039	533,547
	0	0	0	112	1,022	1,358	62,200
UiB-MPFA	1	0	0	756	9,438	11,706	672,454
	2	0	0	4,576	98,311	112,039	7,481,237
	0	0	0	112	1,022	3,905	24,435
UiB-MVEM	1	0	0	756	9,438	33,651	222,927
	2	0	0	4,576	98,311	326,561	2,259,630
	0	0	0	112	1,022	3,905	24,435
UiB-RTO	1	0	0	756	9,438	33,651	222,927
	2	0	0	4,576	98,311	326,561	2,259,623
	0	0	0	100	1,000	1,100	22,626
USTUTT-MPFA	1	0	0	400	9,600	10,000	227,354
	2	0	0	3,600	108,000	111,600	2,731,104
	0	0	0	193	3,400	3,593	17,373
USTUTT-TPFA_Circ	1	0	0	448	9,085	9,533	46,505
	2	0	0	2,582	104,578	107,160	530,224
	0	0	0	100	1,000	4,400	51,720
LANL-MFD	1	0	0	400	8,000	34,840	390,840
	2	0	0	1,600	64,000	267,280	3,035,280
	0	0	0	625	9,572	1,840	25,539
NCU_TW-Hybrid_FEM	1	0	0	2,453	65,934	11,537	169,937
	2	0	0	22,262	638,332	104,581	1,603,776
	0	0	0	81	1,134	1,511	34,085
UNICE_UNIGE-VAG_Cont	1	0	0	361	10,108	11,721	288,933
	2	0	0	1,849	103,544	111,233	2,877,105
	0	0	0	81	1,134	3,870	39,060
UNICE_UNIGE-HFV_Cont	1	0	0	361	10,108	32,319	340,879
	2	0	0	1,849	103,544	320,221	3,454,921
	0	0	0	81	1,134	1,943	43,519
UNICE_UNIGE-VAG_Disc	1	0	0	361	10,108	13,483	328,867
	2	0	0	1,849	103,544	119,771	3,073,987
	0	0	0	81	1,134	4,077	40,041
UNICE_UNIGE-HFV_Disc	1	0	0	361	10,108	33,231	345,135
	2	0	0	1,849	103,544	324,779	3,475,475
	0	0	0	120	1,000	1,617	38,834
ETHZ_USI-FEM_LM	1	0	0	480	10,115	12,714	335,023
	2	0	0	1,920	93,150	103,470	2,775,270
	0	0	0	526	1,054	5,968	11,4924
UNICAMP-Hybrid_Hdiv	1	0	0	2,884	10,589	62,164	1,249,536
	2	0	0	15,052	100,273	604,019	12,448,629
	0	0	0	720	540	1,857	49,417
UNIL_USI-FE_AMR_AFC	1	0	0	10,880	38,180	56,947	1,545,935
	2	0	0	39,520	108,671	579,837	16,878,449
	0	0	0	140	1,000	1,140	7666
INM-EDFM	1	0	0	720	10,000	10,720	73,364
	2	0	0	3,800	100,000	103,800	719,292
	0	0	0	0	1,006	259	3,082
DTU-FEM_COMSOL	1	0	0	0	10,091	1,931	26,771
	2	0	0	0	100,014	17,850	258,202

Table A.8
Computational cost indicators for Case 2.

Method	Refinement	0d cells	1d cells	2d cells	3d cells	dofs	nnz
	0	27	90	252	512	1,820	8,253
UiB-TPFA	1	27	180	1,008	4,096	8,074	43,513
	2	27	360	4,032	32,768	46,622	281,717
	0	27	90	252	512	1,820	8,609
UiB-MPFA	1	27	180	1,008	4,096	8,074	44,984
	2	27	360	4,032	32,768	46,622	287,565
	0	27	90	252	512	4,706	20,795
UiB-MVEM	1	27	180	1,008	4,096	24,862	118,620
	2	27	360	4,032	32,768	161,414	806,000
	0	27	72	226	612	3,970	21,687
UiB-RT0	1	27	159	1,192	5,339	24,727	153,263
	2	27	270	4,536	39,157	148,245	980,955
	0	0	0	284	843	1,127	42,060
USTUTT-MPFA	1	0	0	686	3,076	3,762	207,260
	2	0	0	4,578	38,877	43,455	2,918,322
	0	0	0	312	978	1,290	7,488
USTUTT-TPFA_Circ	1	0	0	1,206	4,286	5,492	31,402
	2	0	0	4,578	38,877	43,455	226,201
	0	0	0	434	628	2,758	23,246
LANL-MFD	1	0	0	1,736	5,024	18,610	150,314
	2	0	0	6,944	40,192	134,812	1,062,572
	0	0	0	252	512	974	22,324
UNICE_UNIGE-VAG_Cont	1	0	0	1,008	4,096	5,902	143,470
	2	0	0	4,032	32,768	39,908	1,014,088
	0	0	0	252	512	2,223	22,599
UNICE_UNIGE-HFV_Cont	1	0	0	1,008	4,096	15,048	157,980
	2	0	0	4,032	32,768	109,368	1,172,592
	0	0	0	252	512	2,102	46,348
UNICE_UNIGE-VAG_Disc	1	0	0	1,008	4,096	10,223	238,891
	2	0	0	4,032	32,768	56,607	1,390,939
	0	0	0	252	512	2,730	24,138
UNICE_UNIGE-HFV_Disc	1	0	0	1,008	4,096	17,076	164,148
	2	0	0	4,032	32,768	117,480	1,197,288
	0	0	0	1,212	512	3,159	67,183
ETHZ_USI-FEM_LM	1	0	0	1,212	4,096	7,343	182,793
	2	0	0	1,212	32,768	38,367	1,036,960
	0	27	69	534	923	6,018	123,312
UNICAMP-Hybrid_Hdiv	1	27	90	1,896	3,912	23,988	479,322
	2	27	249	10,744	38,742	236,868	4,830,288
	0	1,331	2,787	6,513	1,745	16,283	410,491
UNIL_USI-FE_AMR_AFC	1	1,331	5,211	20,673	8,129	45,257	1,180,333
	2	1,331	10,059	72,033	47,553	161,805	4,274,281
	0	0	0	0	550	129	1,561
DTU-FEM_COMSOL	1	0	0	0	3,881	836	10,900
	2	0	0	0	32,147	6,060	84,954

Table A.9
Computational cost indicators for Case 3.

Method	Refinement	0d cells	1d cells	2d cells	3d cells	dofs	nnz
UiB-TPFA	0	0	50	4,305	31,644	44,786	207,295
	1	0	86	13,731	138,446	180,024	849,349
UiB-MPFA	0	0	50	4,305	31,644	44,786	2,596,061
	1	0	86	13,731	138,446	180,024	11,196,843
UiB-MVEM	0	0	50	4,305	31,644	120,696	818,151
	1	0	86	13,731	138,446	496,032	3,438,098
UiB-RTO	0	0	50	4,305	31,644	120,696	818,151
	1	0	86	13,731	138,446	496,032	3,438,098
USTUTT-MPFA	0	0	0	4,321	31,942	36,263	2,459,195
	1	0	0	12,147	131,488	143,635	10,157,331
USTUTT-TPFA_Circ	0	0	0	4,321	31,942	36,263	191,147
	1	0	0	12,147	131,488	143,635	745,375
LANL-MFD	0	0	0	5,617	21,056	75,878	607,730
	1	0	0	22,468	168,448	555,887	4,367,379
UNICE_UNIGE-VAG_Cont	0	0	0	4,321	31,870	10,213	130,781
	1	0	0	7,711	150,083	35,485	479,105
UNICE_UNIGE-HFV_Cont	0	0	0	4,321	31,870	71,708	504,872
	1	0	0	7,711	150,083	319,175	2,206,691
UNICE_UNIGE-VAG_Disc	0	0	0	4,321	31,870	23,302	400,876
	1	0	0	7,711	150,083	59,187	966,849
UNICE_UNIGE-HFV_Disc	0	0	0	4,321	31,870	80,538	532,114
	1	0	0	7,711	150,083	335,599	2,259,971
ETHZ_USI-FEM_LM	0	0	0	750	29,295	33,270	899,809
	1	0	0	3,000	150,930	163,430	4,421,700
UNICAMP-Hybrid_Hdiv	0	0	38	5,580	24,351	153,519	3,180,847
	1	0	51	23,607	162,773	994,243	20,600,135
UNIL_USI-FE_AMR_AFC	0	0	3,877	323,779	68,386	86,594	1,206,048
	1	0	3,877	323,779	547,088	148,993	2,202,947
INM-EDFM	0	0	0	4,036	29,952	33,988	240,398
	1	0	0	10,732	149,760	160,492	1,133,364
DTU-FEM_COMSOL	0	0	0	0	30,984	5,641	80,669
	1	0	0	0	150,524	30,379	469,447
USTUTT-MPFA-refined	5	0	0	49,428	980,212	1,029,640	75,207,825

Table A.10
Computational cost indicators for Case 4.

Method	0d cells	1d cells	2d cells	3d cells	dofs	nnz
UiB-TPFA	0	1,601	52,618	259,409	424,703	1,950,313
UiB-MPFA	0	1,601	52,618	259,409	424,703	22,953,336
UiB-MVEM	0	1,601	52,618	259,409	1,082,740	7,342,691
UiB-RTO	0	1,601	52,618	259,409	1,082,740	7,342,691
USTUTT-MPFA	0	0	52,618	259,420	312,038	21,227,071
USTUTT-TPFA_Circ	0	0	52,618	259,420	312,038	1,721,932
LANL-MFD	0	0	52,070	260,417	783,158	7,953,396
UNICE_UNIGE-VAG_Cont	0	0	52,070	260,431	95,930	1,237,714
UNICE_UNIGE-HFV_Cont	0	0	52,070	260,431	600,561	4,349,901
UNICE_UNIGE-VAG_Disc	0	0	52,070	260,431	252,326	4,497,980
UNICE_UNIGE-HFV_Disc	0	0	52,070	260,431	704,813	4,663,105
ETHZ_USI-FEM_LM	0	0	52,618	212,040	223,532	5,817,930
UNICAMP-Hybrid_Hdiv	0	938	24,853	94,294	629,065	13,233,581
DTU-FEM_COMSOL	0	0	0	1,860,063	319,489	4,709,565

listed as "0d-2d cells" are also three-dimensional cells that correspond to the fractures ("2d"), intersections of fractures ("1d") and intersections of such intersections ("0d").

Supplementary material

Supplementary material associated with this article can be found, in the online version, at doi:10.1016/j.advwatres.2020.103759.

References

Ahmed, E., Jaffré, J., Roberts, J.E., 2017. A reduced fracture model for two-phase flow with different rock types. Math. Comput. Simul. 137, 49–70.

Angot, P., Boyer, F., Hubert, F., 2009. Asymptotic and numerical modelling of flows in fractured porous media. ESAIM: Math. Modell. Numeric. Anal.-Modélisat. Mathématique et Anal. Numér. 43 (2), 239–275.

Arrarás, A., Gaspar, F.J., Portero, L., Rodrigo, C., 2019. Mixed-dimensional geometric multigrid methods for single-phase flow in fractured porous media. SIAM J. Sci. Comput. 41 (5), B1082–B1114. https://doi.org/10.1137/18M1224751.

Barlag, C., Hinkelmann, R., Helmig, R., Zielke, W., 1998. Adaptive methods for modelling transport processes in fractured subsurface systems. 3rd International Conference on Hydroscience and Engineering, Cottbus.

Berre, I., Boon, W., Flemisch, B., Fumagalli, A., Gläser, D., Keilegavlen, E., Scotti, A., Stefansson, I., Tatomir, A., 2018. Call for participation: verification benchmarks for single-phase flow in three-dimensional fractured porous media. arXiv e-prints 1809.06926.

Berre, I., Boon, W. M., Flemisch, B., Fumagalli, A., Gläser, D., Keilegavlen, E., Scotti, A., Stefansson, I., Tatomir, A., Brenner, K., Burbulla, S., Devloo, P., Duran, O., Favino, M., Hennicker, J., Lee, I.-H., Lipnikov, K., Masson, R., Mosthaf, K., Nestola, M. G. C., Ni, C.-F., Nikitin, K., Schädle, P., Svyatskiy, D., Yanbarisov, R., Zulian, P., 2020. Data repository of this work. https://git.iws.uni-stuttgart.de/benchmarks/fracture-flow-3d.git.

Berre, I., Doster, F., Keilegavlen, E., 2019. Flow in fractured porous media: a review of conceptual models and discretization approaches. Transp. Porous Media 130 (1), 215–236. https://doi.org/10.1007/s11242-018-1171-6.

Boon, W.M., Nordbotten, J.M., Yotov, I., 2018. Robust discretization of flow in fractured porous media. SIAM J. Numer. Anal. 56 (4), 2203–2233. https://doi.org/10.1137/17M1139102.

Brenner, K., Groza, M., Guichard, C., Lebeau, G., Masson, R., 2016. Gradient discretization of hybrid dimensional darcy flows in fractured porous media. Numerische Mathematik 134 (3), 569–609. https://doi.org/10.1007/s00211-015-0782-x.

Brenner, K., Hennicker, J., Masson, R., Samier, P., 2016. Gradient discretization of hybrid-dimensional Darcy flow in fractured porous media with discontinuous pressures at matrix-fracture interfaces. IMA J. Numeric. Anal. 37 (3), 1551–1585. https://doi.org/10.1093/imanum/drw044.

Brenner, K., Hennicker, J., Masson, R., Samier, P., 2018. Hybrid-dimensional modelling of two-phase flow through fractured porous media with enhanced matrix fracture transmission conditions. J. Comput. Phys. 357, 100–124.

Brezzi, F., Fortin, M., 1991. Mixed and Hybrid Finite Element Methods. Computational Mathematics, 15. Springer Verlag, Berlin.

Budisa, A., Hu, X., 2019. Block preconditioners for mixed-dimensional discretization of flow in fractured porous media. arXiv e-prints 1905.13513.

Chavent, G., Jaffré, J., 1986. Mathematical models and finite elements for reservoir simulation: Single phase, multiphase and multicomponent flows through porous media. Elsevier Science.

Devloo, P., Teng, W., Zhang, C.-S., 2019. Multiscale hybrid-mixed finite element method for flow simulation in fractured porous media. Comput. Model. Eng. Sci. 119 (1), 145–163. https://doi.org/10.32604/cmes.2019.04812.

Durán, O., Devloo, P.R., Gomes, S.M., Valentin, F., 2019. A multiscale hybrid method for darcy's problems using mixed finite element local solvers. Comput. Methods. Appl. Mech. Eng. 354, 213–244. https://doi.org/10.1016/j.cma.2019.05.013.

Ern, A., Guermond, J.-L., 2004. Theory and Practice of Finite Elements. Applied mathematical sciences, 159. Springer. https://doi.org/10.1007/978-1-4757-4355-5.

Favino, M., Hunziker, J., Caspari, E., Quintal, B., Holliger, K., Krause, R., 2020. Fully-automated adaptive mesh refinement for media embedding complex heterogeneities: application to poroelastic fluid pressure diffusion. Comput. Geosci. 2020. https://doi.org/10.1007/s10596-019-09928-2.

Flemisch, B., Berre, I., Boon, W., Fumagalli, A., Schwenck, N., Scotti, A., Stefansson, I., Tatomir, A., 2018. Benchmarks for single-phase flow in fractured porous media. Adv. Water Resour. 111, 239–258. https://doi.org/10.1016/j.advwatres.2017.10.036.

Fumagalli, A., Keilegavlen, E., Scialò, S., 2019. Conforming, non-conforming and non-matching discretization couplings in discrete fracture network simulations. J. Comput. Phys. 376, 694–712. https://doi.org/10.1016/j.jcp.2018.09.048.

Geuzaine, C., Remacle, J.-F., 2009. Gmsh: a 3-d finite element mesh generator with built-in pre- and post-processing facilities. Int. J. Numer. Methods Eng. 79 (11), 1309–1331. https://doi.org/10.1002/nme.2579.

Gläser, D., 2020. Case1 - Single Fracture. 10.18419/darus-862.

Keilegavlen, E., Berge, R., Fumagalli, A., Starnoni, M., Stefansson, I., Varela, J., Berre, I., 2020. PorePy: an open-Source software for simulation of multiphysics processes in fractured porous media. Comput. Geosci.. https://doi.org/10.1007/s10596-020-10002-5.

Koch, T., Gläser, D., Weishaupt, K., Ackermann, S., Beck, M., Becker, B., Burbulla, S., Class, H., Coltman, E., Emmert, S., Fetzer, T., Grüninger, C., Heck, K., Hommel, J., Kurz, T., Lipp, M., Mohammadi, F., Scherrer, S., Schneider, M., Seitz, G., Stadler, L., Utz, M., Weinhardt, F., Flemisch, B., 2020. DuMux 3 - an open-source simulator for solving flow and transport problems in porous media with a focus on model coupling. Comput. Math. Appl. 2020. https://doi.org/10.1016/j.camwa.2020.02.012.

Krause, R., Zulian, P., 2016. A parallel approach to the variational transfer of discrete fields between arbitrarily distributed unstructured finite element meshes. SIAM J. Sci. Comput. 38, C307–C333. https://doi.org/10.1137/15M1008361.

Kumar, K., List, F., Pop, I.S., Radu, F.A., 2020. Formal upscaling and numerical validation of unsaturated flow models in fractured porous media. J. Comput. Phys. 407, 109138.

Kuzmin, D., Löhner, R., Turek, S. (Eds.), 2012. Flux-corrected transport: Principles, algorithms, and applications. Springer. https://doi.org/10.1007/978-94-007-4038-9.

Köppel, M., Martin, V., Jaffré, J., Roberts, J.E., 2019. A lagrange multiplier method for a discrete fracture model for flow in porous media. Comput. Geosci. 23 (2), 239–253. https://doi.org/10.1007/s10596-018-9779-8.

Köppel, M., Martin, V., Roberts, J.E., 2019. A stabilized lagrange multiplier finite-element method for flow in porous media with fractures. GEM - Int. J. Geomath. 10 (1), 7. https://doi.org/10.1007/s13137-019-0117-7.

Lee, I.-H., Ni, C.-F., 2015. Fracture-based modeling of complex flow and CO2 migration in three-dimensional fractured rocks. Comput. Geosci. 81, 64–77. https://doi.org/10.1016/j.cageo.2015.04.012.

Lee, I.-H., Ni, C.-F., Lin, F.-P., Lin, C.-P., Ke, C.-C., 2019. Stochastic modeling of flow and conservative transport in three-dimensional discrete fracture networks. Hydrol. Earth Syst. Sci. 23, 19–34. https://doi.org/10.5194/hess-23-19-2019.

Lipnikov, K., Manzini, G., Shashkov, M., 2014. Mimetic finite difference method. J. Comput. Phys 257, 1163–1227. https://doi.org/10.1016/j.jcp.2013.07.031.

List, F., Kumar, K., Pop, I.S., Radu, F.A., 2020. Rigorous upscaling of unsaturated flow in fractured porous media. SIAM J. Math. Anal. 52 (1), 239–276.

Martin, V., Jaffré, J., Roberts, J.E., 2005. Modeling fractures and barriers as interfaces for flow in porous media. SIAM J. Sci. Comput. 26 (5), 1667–1691. https://doi.org/10.1137/S1064827503429363.

Nikitin, K.D., Yanbarisov, R.M., 2020. Monotone embedded discrete fractures method for flows in porous media. J. Comput. Appl. Math. 364, 112353. https://doi.org/10.1016/j.cam.2019.112353.

Nordbotten, J.M., Boon, W.M., Fumagalli, A., Keilegavlen, E., 2019. Unified approach to discretization of flow in fractured porous media. Comput. Geosci. 23 (2), 225–237. https://doi.org/10.1007/s10596-018-9778-9.

Odsæter, L.H., Kvamsdal, T., Larson, M.G., 2019. A simple embedded discrete fracture-matrix model for a coupled flow and transport problem in porous media. Comput. Methods Appl. Mech. Eng. 343, 572–601. https://doi.org/10.1016/j.cma.2018.09.003.

Raviart, P.A., Thomas, J.M., 1977. A mixed finite element method for 2-nd order elliptic problems. In: Galligani, I., Magenes, E. (Eds.), Mathematical Aspects of Finite Element Methods. Springer Berlin Heidelberg, pp. 292–315. https://doi.org/10.1007/BFb0064470.

Roberts, J.E., Thomas, J.-M., 1991. Mixed and hybrid methods. In: Ciarlet, P.G., Lions, J.L. (Eds.), Handbook of Nnumerical Analysis, Vol. II. North-Holland, Amsterdam, pp. 523–639. https://doi.org/10.1016/S1570-8659(05)80041-9.

Schädle, P., Zulian, P., Vogler, D., Bhopalam, S.R., Nestola, M.G., Ebigbo, A., Krause, R., Saar, M.O., 2019. 3d non-conforming mesh model for flow in fractured porous media using lagrange multipliers. Comput. Geosci. 132, 42–55. https://doi.org/10.1016/j.cageo.2019.06.014.

Zielke, W., Helmig, R., Krohn, K., Shao, H., Wollrath, J., 1991. Discrete modelling of transport processes in fractured porous rock. In: 7th ISRM Congress, pp. 57–60.

Zulian, P., Kopanicáková, A., Nestola, M. C. G., Fink, A., Fadel, N., Magri, V., Schneider, T., Botter, E., 2016. Utopia: a C++ embedded domain specific language for scientific computing. Git repository.